1521-0111/104/1/1–16$35.00
MOLECULAR PHARMACOLOGY

dx.doi.org/10.1124/molpharm.122.000641
Mol Pharmacol 104:1–16, July 2023

Multiomics Analyses Identify Proline Endopeptidase–Like Protein As a Key Regulator of Protein Trafficking, a Pathway Underlying Alzheimer's Disease Pathogenesis[S]

Mariana Lemos Duarte,[4] Minghui Wang,[4] Ivone Gomes,[4] Chenge Liu,[1] Ali Sharma,[2] Amanda K. Fakira,[3] Achla Gupta, Seshat M. Mack, Bin Zhang, and Lakshmi A. Devi

Department of Pharmacological Sciences (M.L.D., I.G., C.L., A.S., A.K.F., A.G., S.M.M., L.A.D.), Department of Genetics and Genomics (M.W., B.Z.), and Department of Neurology (M.L.D.), Icahn School of Medicine at Mount Sinai, New York, New York

Received October 24, 2022; accepted April 12, 2023

ABSTRACT

Current treatments for Alzheimer's disease (AD) help reduce symptoms for a limited time but do not treat the underlying pathology. To identify potential therapeutic targets for AD, an integrative network analysis was previously carried out using 364 human postmortem control, mild cognitive impairment, and AD brains. This analysis identified proline endopeptidase–like protein (PREPL), an understudied protein, as a downregulated protein in late-onset AD patients. In this study we investigate the role of PREPL. Analyses of data from human postmortem samples and PREPL knockdown (KD) cells suggest that PREPL expression modulates pathways associated with protein trafficking, synaptic activities, and lipid metabolism. Furthermore, PREPL KD impairs cell proliferation and modulates the structure of vesicles, levels of neuropeptide-processing enzymes, and secretion of neuropeptides. In addition, decrease in PREPL levels leads to changes in the levels of a number of synaptic proteins as well as changes in the levels of secreted amyloid beta (Aβ) 42 peptide and Tau phosphorylation. Finally, we report that local decrease in PREPL levels in mouse hippocampus attenuates long-term potentiation, suggesting a role in synaptic plasticity. Together, our results indicate that PREPL affects neuronal function by modulating protein trafficking and synaptic function, an important mechanism of AD pathogenesis.

SIGNIFICANCE STATEMENT

Integrative network analysis reveals proline endopeptidase–like protein (PREPL) to be downregulated in human sporadic late-onset Alzheimer's disease brains. Down regulation of PREPL leads to increases in amyloid beta secretion, Tau phosphorylation, and decreases in protein trafficking and long-term potentiation.

Introduction

Alzheimer's disease is one of the most common forms of dementia, affecting nearly 5.8 million people in the US in 2020 (Matthews et al., 2019). It is projected that by 2040, the treatment of AD in the US will cost ~$500 billion annually (Hurd et al., 2013). Unfortunately to date, the cellular and molecular basis of AD pathogenesis remain largely unknown and no effective treatment is available to prevent, stop, or delay AD progression.

Two major pathologic hallmarks of AD have been extensively studied: 1) the extracellular amyloid plaques derived from aggregation of amyloid beta (Aβ) peptides and 2) intraneuronal neurofibrillary tangles (NFTs) caused by Tau hyperphosphorylation (Spires-Jones and Hyman, 2014). These pathologic hallmarks have been associated with synaptic loss in the central cortex and hippocampus and subsequent memory impairments (Oboudiyat et al., 2013). Beyond these two mainly studied molecular markers of AD, the cellular and molecular basis of AD pathogenesis remain largely unknown, and novel therapeutic strategies for AD are urgently needed for better disease management.

Recent studies revealed the existence of a unique set of genetic risk factors for late-onset AD (LOAD) (Zhang et al., 2013).

This research was funded by National Institutes of Health National Institute on Drug Abuse [Grant DA008863], National Institute of Neurologic Disorders and Stroke [Grant NS026880], and National Center for Advancing Translational Sciences [Grant 1R03TR003647-01] (to L.A.D.); National Institute on Aging [Grant U01AG046170] (to B.Z.); and National Institute on Drug Abuse diversity supplement [Grant DA008863S] (to S.M.M.).
The authors do not have any conflicts of interest to disclose.
[1]Current affiliation: Program of Pharmacology, Weill Graduate School of Medical Sciences, Cornell University, Ithaca, New York.
[2]Current affiliation: National Institute on Aging, Washington, DC.
[3]Current affiliation: Department of Biomedical Sciences, Cooper Medical School of Rowan University, Camden, New Jersey.
[4]M.L.D., M.W., and I.G. contributed equally to this work.
dx.doi.org/10.1124/molpharm.122.000641.
[S] This article has supplemental material available at molpharm.aspetjournals.org.

ABBREVIATIONS: Aβ, amyloid beta; ABE, acyl-biotin exchange; AD, Alzheimer's disease; AP-1, adaptor protein complex-1; DEG, differentially expressed gene; ELISA, enzyme-linked immunosorbent assay; eQTL, expression quantitative trait locus; FDR, false discovery rate; fEPSP, field excitatory postsynaptic potential; GO, gene ontology; HAM, hydroxylamine; HBSS, Hank's balanced salt solution; IF, immunofluorescence; KD, knockdown; LOAD, late-onset Alzheimer's disease; LTP, long-term potentiation; MSBB, Mount Sinai Biobank; NEM, N-ethylmaleimide; NFT, neurofibrillary tangle; ODN, oligodeoxynucleotide; PC1, proprotein convertase 1; PC2, proprotein convertase 2; PPR, paired-pulse ratio; PREPL, proline endopeptidase–like protein; qPCR, quantitative polymerase chain reaction; RNA-seq, RNA sequencing; TF, transcription factor; WGS, whole-genome sequencing.

These genetic risk loci seem to cluster in patterns associated with genes related to immune responses, lipid processing, and endocytosis (Bettens et al., 2013). To characterize molecular markers responsible for AD progression, studies performed under the Accelerating Medicine Partnership Program for Alzheimer's Disease (AMP-AD) Consortium using human brain samples from the National Institute on Aging and the Mount Sinai Brain Bank Alzheimer's Disease Cohort predicted causal regulators for Alzheimer's disease (Wang et al., 2018). Data were extracted from whole genome sequencing, whole exome sequencing, RNA-sequencing, and proteome profiling from multiple regions of 364 human postmortem control, mild cognitive impairment (MCI), and AD brains, with rich clinical and pathophysiological information (Zhang et al., 2013; Zhang and Zhu, 2013; Wang et al., 2018; Beckmann et al., 2020). The resulting multiscale network modeling analysis identified potential key regulators of AD pathogenesis, including proline endopeptidase–like protein (PREPL) (Zhang et al., 2013; Zhang and Zhu, 2013; Beckmann et al., 2020; Wang et al., 2021).

PREPL, a protein reported to be downregulated in late-onset AD patients (Zhang et al., 2013; Beckmann et al., 2020; Wang et al., 2021), is highly expressed in the brain and at reduced levels in skeletal muscle, heart, and kidneys (Régal et al., 2018). In mouse brain, PREPL is expressed in regions related to learning, memory, coordination of motor function, and modulation of arousal (Morawski et al., 2013). PREPL is thought to play an important role in executing higher cognitive commands (D'Agostino et al., 2013), and thus PREPL deficiency in AD could ultimately contribute to the disease development.

Previous studies reported that PREPL deficiency is associated with a recessive metabolic disorder known as congenital myasthenic syndrome-22. Patients with this condition suffer from severe neonatal hypotonia, eyelid ptosis, feeding problems, and growth hormone deficiency (Régal et al., 2014, 2018). Recent studies to explore the mechanism of action of PREPL led to the observation that there are two isoforms and that they exhibit distinct subcellular localizations. The longer isoform, $PREPL_l$, has mitochondrial localization and plays a role in maintaining mitochondrial homeostasis (Rosier et al., 2021). The shorter isoform, $PREPL_s$, has cytosolic localization, interacts with clathrin-associated adaptor protein complex-1 (AP-1), and affects vesicular trafficking. The molecular mechanism by which PREPL functions is unknown, although a recent study has suggested that it could function as a depalmitoylating enzyme due to its (thio)esterase activity (Rosier et al., 2021).

Here we began to investigate the role of PREPL dysregulation in AD and the mechanisms by which PREPL deficiency could contribute to the AD pathophysiology. Our results suggest that PREPL is progressively downregulated in brain samples with higher clinical dementia scores. Using multiomics analysis, we found that PREPL expression modulates pathways related to synaptic processes, protein trafficking, and lipid metabolism. PREPL knockdown (KD) impairs cell proliferation, disrupts intracellular vesicle structures, and modulates expressions of key neuropeptide processing enzymes, vesicle-associated membrane proteins, and secreted neuropeptides. PREPL KD increases extracellular levels of Aβ 42 peptide and Tau phosphorylation. Finally, we show that local decreases in PREPL expression in hippocampus correlate with attenuation of long-term potentiation. Taken together, our results indicate PREPL as a novel player in AD pathogenesis.

Materials and Methods

Antibodies. Anti-golgin-97 (#A21270; Invitrogen); anti-adaptin-gamma (#610386; BD Transduction Laboratory); anti-calnexin (#2679; Cell Signaling); anti-actin (#A4700; Sigma); anti-alpha-tubulin (#A11126; Invitrogen); anti-beta-tubulin III (#T8660; Sigma); anti-TGN38 (#MA3-063, Invitrogen; #85181S, Cell Signaling); anti-GAPDH (#MA5-15738; Invitrogen); anti-PREPL (#SAB1401484; Sigma); anti-Rab5 (#3547T; Cell Signaling); anti-Rab7 (#9367T, Cell Signaling); anti-Rab9 (#5133S; Cell Signaling); total Tau (#AVG702-A11, antigenic sequence G(D)RSGYSSPGSPGTPGSRSRT; AvantGen); phospho Tau S491 (#AVG702P-G11, antigenic sequence G(D)RSGYS(pS)PGSPGTPGSRSRT; AvantGen); phospho Tau S554 (#AVG704P-B9, antigenic sequence (K)SKIG(pS)TENLKHQPGGG; AvantGen); phospho Tau S698 (#AVG705P-G12, antigenic sequence KTDHGAEIVYK(pS)PVVSGD; AvantGen); monoclonal antibody to human Tau (#MN1000; Thermo Fisher); anti-rabbit horseradish peroxidase (HRP) (#PI-1000; Vector); anti-mouse HRP (#PI-2000; Vector); anti-rabbit IRDye 680CW (#926-32223; LI-COR); anti-rabbit IRDye 800CW (#926-32213; LI-COR); anti-mouse IRDye 680CW (#925-68070; LI-COR); IRDye Streptavidin 800CW (#926-32230; LI-COR); goat anti-rabbit Alexa Fluor 568 (#A11011; Invitrogen); goat anti-mouse Alexa Fluor 488 (#A11001; Invitrogen); and goat anti-mouse Alexa Fluor 568 (#A11031; Invitrogen).

shRNA Sequences. shPREPL_A (AATACACGGAATGCTTTACTATGTTGAGCAT); shPREPL_D (CGAGTGCCGCTGAAAGGAATCGTGAACTA); Scramble (GGGTGAACTCACGTCAGAA); shTAU (GACAGAGTCCAGTCGAAGATT).

Bayesian Network Analysis. We focused on network analysis using transcriptomic data from the human parahippocampal gyrus (PHG) region, as it has been identified as the most vulnerable region to LOAD pathology in the Mount Sinai Biobank cohort according to our pancortical selective vulnerability analysis in LOAD (Wang et al., 2016). Bayesian causal network was constructed by integrating genome-wide gene expression, whole-genome sequencing (WGS) single-nucleotide polymorphism (SNP) genotype, and known transcription factor (TF)-target relationships. Briefly, we first computed expression quantitative trait loci (eQTLs) and then employed a formal statistical causal inference test (CIT) (Millstein et al., 2009) to infer the causal probability between gene pairs associated with the same eQTL. The causal relationships inferred were used, together with TF-target relationships from the ENCODE project, as structural priors for building a causal gene regulatory network from the gene expression data through a Monte Carlo Markov Chain (MCMC) simulation-based procedure (Zhu et al., 2007). We followed a network averaging strategy in which 1000 networks were generated from the MCMC procedure starting with different random structures, and links that were shared by more than 30% of the networks were used to define a final consensus network structure. To ensure that the consensus network is a directed acyclic graph, an iterative deloop procedure was conducted, removing the most weakly supported link from all links involved in any loop. Following Zhang et al. (2013), we performed key driver analysis (KDA) on the consensus Bayesian network to identify key hub genes that regulated a large number of downstream nodes. We used existing software tool RIMBANet for constructing the Bayesian network. The software tool and sample usage are available at https://labs.icahn.mssm.edu/zhulab/software/. An easy-to-use pipeline for running RIMBANet is available from GitHub at https://github.com/mw201608/BayesianNetwork.

PREPL-Centric Differential Pathway Correlation Analysis. To test if any particular gene ontology (GO) pathway showed differential mRNA gene expression correlation with *PREPL* in AD brains, we first computed the Spearman's correlation between *PREPL* and all other genes annotated in the GO/pathway gene sets

curated in the MSigDB (v6.1) for demented brains (CDR $\geq$1) and nondemented control brains (CDR $<$1) of the Mount Sinai Biobank (MSBB) cohort separately. Then for each GO/pathway gene set, the Wilcoxon paired rank sum test was employed to compare the PREPL-centric correlation coefficients (r) between demented and nondemented control brains. *P* value significance was adjusted by false discovery rate.

RNA Sequencing Analyses. The pair-ended raw sequencing reads were aligned to mouse mm10 genome using STAR aligner (version 2.5.3a). After read alignment, featureCounts (v1.4.6) was used to quantify expression at the gene level based on the GENCODE gene model GRCm38.p5 release M15. Genes with at least 1 count per million (cpm) in at least one sample were considered expressed and hence retained for further analysis; others were removed. The gene read counts data were normalized using the trimmed mean of M-values normalization (TMM) method (Robinson and Oshlack, 2010) to adjust for sequencing library size differences. Hierarchical cluster analysis was performed using R programming language. Differential gene expression between sample groups was calculated by a linear model analysis using the Bioconductor package limma (Law et al., 2014; Ritchie et al., 2015). To adjust for multiple tests, false discovery rate (FDR) was estimated using the Benjamini-Hochberg (BH) method (Hochberg and Benjamini, 1990). Genes showing at least 1.2-fold changes and FDR-adjusted *P* values less than 0.05 were considered significant. Gene functional enrichment analysis was executed using hypergeometric test based on Broad Institute's MSigDB annotation (Subramanian et al., 2005).

Mass Spectrometry Sample Preparation and Data Analysis. Neuro2A wild-type and shPREPL A knockdown cells were pelleted at a concentration of 250,000 cells per tube. After three washes with PBS containing protease and phosphatase inhibitors, the cell pellet was fast frozen on dry ice. A total of three samples per condition was subjected to proteomic analysis at the Yale/NIDA Neuroproteomics Center essentially as described (Mansuri et al., 2020). The MS/MS spectra analysis and the protein identification were performed essentially as described (Hirosawa et al., 1993; Perkins et al., 1999) using the Mascot Distiller program (Perkins et al., 1999). Proteins with 2+ unique peptides and $P < 0.005$ were selected. The determination of protein normalized abundance was calculated using Progenesis QI v3.0 software. Similar to differential gene expression, linear model implemented in *limma* (Ritchie et al., 2015) was used to compute differential protein expression between sample groups and then FDR was estimated using BH method (Hochberg and Benjamini, 1990). Proteins showing at least 1.2-fold changes and FDR-adjusted *P* values less than 0.05 were considered significant. Functional enrichment analysis was performed using hypergeometric test based on Broad Institute's MSigDB annotation (Subramanian et al., 2005).

Cell Culture and Transfection. Neuro2A (N2A) and HT22 cells were cultured at 37°C and 5% CO_2 in Dulbecco's modified Eagle's medium (DMEM) supplemented with 10% fetal bovine serum and 1% penicillin-streptomycin. piLenti-shRNA-GFP vectors expressing mouse PREPL shRNA and scrambled shRNA were purchased from ABM Good Inc. Tau shRNA was purchased from Sigma-Aldrich. To generate PREPL knockdown and Tau knockdown cells, N2A or HT22 cells were transfected with PREPL shRNA (either shRNA A or D) or Tau shRNA using TurboFect transfection reagent (#RO534; Thermo Fisher) according to the manufacturer's protocol. After 48 hours, positively transfected cells were selected by adding puromycin at a final concentration of 1.6 μg/ml. Monoclonal cell populations were generated by limiting dilution. For this, transfected cells were removed from the culture plate by trypsinization and single-cell suspensions were generated by up and down pipetting through a serological pipette. Cells were then diluted and seeded into a 96-well plate at a density of 1 cell per well. As cells expanded to confluency, the different clones were assessed by quantitative polymerase chain reaction (qPCR) and immunofluorescence (IF) imaging to select the clones with effective PREPL or Tau knockdown. We used N2A and HT22 wild-type cells transfected with scramble shRNA as controls. Cell lines with PREPL-specific shRNA (construct A or D) knockdown are considered as experimental conditions. For PREPL rescue experiments, cell lines with PREPL-specific shRNA knockdown were transfected with human PREPL GFP (clone ID: OHu11820C; GenScript) using TurboFect transfection reagent and cells were grown in the presence of puromycin (1.6 μg/ml) and G418 (500 μg/ml). N2A cells stably expressing amyloid precursor protein (N2A APP) were generated using TurboFect transfection reagent (#RO534; Thermo Fisher) according to the manufacturer's protocol; cells were grown in the presence of 500 μg/ml G418.

Quantitative Polymerase Chain Reaction. For the qPCR analysis, the mRNA was extracted from the cells as described by the manufacturer (#74104; Qiagen). cDNA synthesis was carried out using SuperScript IV VILO (#11754050; Thermo Fisher) and 2 μg of RNA as described by the manufacturer. The qPCR reaction was carried out as described by the manufacturer (#204143; Qiagen) using the PREPL Primers (FW: TGGAGAGCTTCGGTTTCTCG and RV: CTTGGCAGGCGGGACTTAAT) at a final concentration of 100 nM and the cDNA at a concentration of 2.5 ng/μl. The qPCR reaction used SYBR Green dye, and the plate was read at the qPCR Core Facility at Mount Sinai.

Live Cell Imaging. For phase-contrast microscopy, 10-cm^2 dishes (#430167; Corning) containing N2A cells or corresponding PREPL KD cells in growth media lacking phenol red were imaged at 20× magnification using a Zeiss Vert A1 microscope. For confocal microscopy, 35-mm glass bottom dishes with a 14-mm microwell (#P35G-1.0-14-C; MatTek) were pretreated with poly-D-lysine (#P0899; Sigma-Aldrich) for 1 hour at room temperature, washed three times with PBS (5 minutes each), air-dried, and sterilized overnight under UV light in a tissue culture hood. N2A cells and corresponding PREPL KD cells (5000 cells) were seeded into the 14-mm microwell and allowed to attach. The next day, cells were incubated overnight at 37°C with 1:200 dilution of CellBrite red cytoplasmic membrane dye (#30023; Biotium). Staining media was removed, and cells were washed three times (5 minutes each wash) with growth media without phenol red. Cells were imaged using a Zeiss LSM 880 confocal microscope with a 63× oil lens for a final magnification of 100×.

Confocal Microscopy. N2A and corresponding PREPL KD cells (5000 cells) were seeded into poly-D-lysine–coated 35-mm glass-bottom dishes with a 14-mm microwell and allowed to attach overnight in complete growth media. Cells were rinsed with sterile PBS for 5 minutes, fixed with 4% paraformaldehyde in PBS (pH 7.4) for 15 minutes, and washed twice with cold sterile PBS. Cells were permeabilized using 0.2% Triton-X-100 in PBS for 10 minutes, followed by three washes (5 minutes each) with PBS. Cells were incubated with 1 ml blocking buffer [PBS containing 0.2% Triton-X-100 and 2% normal goat serum (#005-000-121; Jackson ImmunoResearch Laboratories)] for 1 hour at room temperature, followed by overnight incubation at 4°C with anti-PREPL antibodies (1:500 in blocking buffer for N2A cells) and with antibodies to intracellular vesicle markers (1:200 in blocking buffer for N2A cells and corresponding PREPL KD cells). Cells were washed three times with sterile PBS (5 minutes each wash) and incubated for 90 minutes at room temperature (protected from light exposure) with 1:1000 dilution (in blocking buffer) of goat anti-rabbit Alexa Fluor 568 (#A11011; Invitrogen) or goat anti-mouse Alexa Fluor 488 (Invitrogen, #A11001). Cells were washed three times with sterile PBS (10 minutes each wash) followed by the addition of Pro-Long TM Gold antifade reagent with DAPI (#P36931; Invitrogen), kept at room temperature for 2 hours in the dark followed by storage at 4°C until imaging. Cells were imaged using a Zeiss LSM 880 confocal microscope with a 63× oil lens for a final magnification of 100×.

Cell Proliferation and Clonogenic Assays. HT22, N2A cells, and corresponding PREPL KD cells were seeded into 24-well Falcon polystyrene plates (#353047) at 15,000 cells per well. Every 24 hours, cells were stained with 0.2% Trypan Blue (#15250061; Gibco), and cell numbers were counted in triplicate using a hemocytometer. In

the rescue proliferation assay, the PREPL-GFP construct was overexpressed in the N2A PREPL KD cells, and 24 hours later the cells were counted as described above. In experiments examining the effect of palmostatin M (#B1193294; BenchChem), an acyl protein thioesterase inhibitor that blocks PREPL activity (Rosier et al., 2021), N2A cells (10,000 cells per well) were treated with either 20 μM or 50 μM palmostatin M and cells were counted as described above after 24, 48, and 72 hours. Clonogenic assays were performed in six-well plates with N2A wild-type and PREPL KD cells. Cells were seeded at ~200 cells per well and stained with crystal violet (0.5% w/v) after 3 weeks. The number of colonies was then counted.

Cellular Enzyme-Linked Immunosorbent Assay. A total of 1×10^5 cells per well was seeded on high-binding polystyrene 96-well plates (#3361; Corning). After 24 hours, the culture medium was removed and cells were blocked with phosphate-buffered saline (PBS) containing 3% bovine serum albumin (BSA) and 0.1% Triton-X-100 for 60 minutes at room temperature. After the blocking buffer was aspirated, cells were incubated with primary antibodies (1:1000 dilution in PBS/1% BSA) at 4°C overnight. The next day, wells were washed three times for 15 minutes with PBS. Cells were then incubated with the respective secondary antibodies coupled to horseradish peroxidase (1:1000 dilution in PBS) for 90 minutes at room temperature. The substrate, o-phenylenediamine (OPD), was added at a concentration of 5 mg OPD per 10 ml of citric phosphate buffer (0.15 M citric acid, 0.15M dibasic sodium phosphate, pH 5.0) containing 20 μl hydrogen peroxide. The reaction was terminated by the addition of 5N H_2SO_4, and the absorbance at 490 nm was measured with a Bio-Rad enzyme-linked immunosorbent assay (ELISA) plate reader.

Secretion Assay. Cells were seeded at 40%–60% confluency on poly-D-lysine–coated 24-well plates. The wells were rinsed twice with Mg^{2+}/Ca^{2+}-free PBS. Cells were then incubated at 37°C with modified Mg^{2+}/Ca^{2+}-free Krebs-Ringer-HEPES–buffered basal medium (KRH-basal: 25 mM HEPES pH 7.4, 125 mM NaCl, 4.8 mM KCl, 1.2 mM KH_2PO_4, 5.6 mM glucose, 0.1% BSA, 1× Pierce protease inhibitor cocktail) containing 1 mM $CoCl_2$. Cells were then rinsed and incubated with KRH-Basal solution without $CoCl_2$ for 30 minutes at 37°C. The KRH-basal was collected, and the cells were then treated with a depolarizing KRH buffer for 30 minutes at 37°C (KRH-depolarizing: 25 mM HEPES pH 7.4, 80 mM NaCl, 51 mM KCl, 1.2 mM KH_2PO_4, 5.6 mM glucose, 0.1% BSA, 5.2 mM $CaCl_2$, 2 mM $CoCl_2$, 1× Pierce protease inhibitor cocktail). The KRH-depolarizing was also collected. The collected KRH-basal and KRH-depolarizing supernatants were added (75 μl per well) into Corning 9018 96-well plates and dried off at 37°C for 48 hours. ELISA assays to detect secreted levels of neuropeptide AQEE were carried using an anti-AQEE antibody (Chakraborty et al., 2006) as described under cellular ELISA assays.

Receptor Internalization Assay. These were carried out essentially as described previously (Mack et al., 2022). Briefly, $1.5–2 \times 10^5$ cells per well were seeded on 24-well poly-D-lysine–coated plates. After 48 hours, wells were gently washed with cold 1× PBS and incubated on ice for 60 minutes with cannabinoid 1 receptor (CB_1R) (Gupta et al., 2007) or delta opioid receptor (DOR) antibodies (1:1000 dilution in PBS containing 1% BSA) (Gupta et al., 2007; Bushlin et al., 2012). Cells were then treated with 100 nM HU210 or 1 μM deltorphin II for indicated times at 37°C. After removing the agonist solution, cells were fixed with 4% paraformaldehyde for 3 minutes and washed with PBS before adding the secondary antibodies coupled to horseradish peroxidase. Absorbance at 490 nm was measured with a Bio-Rad ELISA reader. In experiments examining the effect of palmostatin M, cells were pretreated with 20 μM palmostatin M for 30 minutes and receptor internalization was carried out as described above in the presence of palmostatin M.

Immunofluorescence Assay. HT22, N2A, and corresponding shPREPL cells were seeded at 10,000 cells per well into 96-well plates. After 24 hours, cells were incubated with 4% paraformaldehyde (100 μl per well) for 20 minutes for fixation and washed three times with 1× Hank's balanced salt solution (HBSS). Cells were then permeabilized with ice-cold 100% methanol (100 μl per well) for 10 minutes and washed three times with 1× HBSS. Blocking buffer (5% FBS, 0.01% saponin in HBSS) was added (100 μl per well) for 1 hour. Primary antibodies were added at 1:500 dilution, and incubation was carried out at 4°C overnight. The next day, cells were washed three times with blocking buffer followed by incubation with Alexa Fluor secondary antibodies (Thermo Fisher) at 1:1000 dilution for 90 minutes at room temperature. Cells were triple washed with 1× HBSS and incubated with DAPI (0.5 $\mu g/\mu l$) for 5 minutes. Immunofluorescence signals were read in the IN Cell (GE Healthcare) plate-reader microscope with 20× objective and five fields per well. The immunofluorescence (IF) analysis was conducted using ImageJ and Cell Profiler. For the ImageJ analyses, the region of interest was selected individually in the bright field and the signal intensity was measured in the corresponding IF images. The background noise was subtracted using 50 pixels roll ball radius. Four separate fields for a total of ~100 cells were measured for each condition. For the Cell Profiler analyses, we used the protocol described in Lemos Duarte et al. (2021).

Field Electrophysiology. Male C57BL/6J wild-type mice (Jackson Laboratories) aged 6–8 weeks were used in these studies. Animals were anesthetized with isoflurane following the Icahn School of Medicine at Mount Sinai Animal Care and Use Committee (IACUC)-approved protocol. We used the protocol described by Blitzer et al. (1998) and Tsokas et al. (2005) to obtain acute coronal slices of dorsal hippocampus. Briefly, brains were rapidly removed from the skull and placed in an ice-cold modified ACSF solution containing (in mM): 215 sucrose, 2.5 KCl, 1.6 NaH_2PO_4, 4 $MgSO_4$, 1 $CaCl_2$, 4 $MgCl_2$, 20 glucose, 26 $NaHCO_3$ (pH 7.4 equilibrated with 95% O_2 and 5% CO_2). Coronal brain slices (400 μm thick) were prepared with a Vibratome VT1200S (Leica Microsystems, Germany) and then incubated at room temperature in a physiologic ACSF containing (in mM): 120 NaCl, 3.3 KCl, 1.2 Na_2HPO_4, 26 $NaHCO_3$, 1.3 $MgSO_4$, 1.8 $CaCl_2$, 11 glucose (pH 7.4 equilibrated with 95% O_2 and 5% CO_2). The hemislices were transferred to a recording chamber perfused with ACSF at a flow rate of ~2 ml/min using a peristaltic pump. All recordings were performed using a MultiClamp 700B amplifier and Digidata 1440A (Molecular Devices). Field excitatory postsynaptic potentials (fEPSPs) were evoked by activating Schaffer collaterals with a patch-type pipette (monopolar stimulation) filled with ACSF and placed in the middle third of stratum radiatum 150–200 μm away from the recording pipette and at approximately the same slice depth (150–200 μm). Square-wave current pulses (100 μs pulse width) were delivered by ISO-Flex stimulator (AMPI). At the start of each experiment, an input-output (I-O) curve was constructed by recording fEPSPs in response to increasing stimulus strength (1–6 μA). Three fEPSPs per stimulus strength were recorded with intervals of 20 seconds between stimulations, starting with the lowest intensity. The average slope of each fEPSP (in mV/ms) for each stimulus intensity versus the amplitude of the fiber volley was plotted. After construction of an I-O curve, a stimulus intensity that evoked a fEPSP at 70% of the spike threshold was used in paired-pulse ratio (PPR) experiments. To evaluate PPR, paired stimuli were delivered every 60 seconds with decreasing interstimulus intervals (100, 50, and 20 milliseconds). Each interstimulus interval was repeated three times, and the resulting potentials were averaged. The ratio of the average amplitude of fEPSP2/fEPSP1 was calculated. For long-term potentiation (LTP) experiments, a baseline response was recorded for 20 minutes and then LTP was induced by theta-burst stimulation (TBS: four pulses at 100 Hz repeated with 10-millisecond interburst intervals). Differences in the average slope during the last five minutes of the 1-hour recording between scrambled and PREPL oligodeoxynucleotide (ODN) groups were compared for statistical analysis.

Surgery and Oligodeoxynucleotide Injections. Bilateral hippocampal surgeries (4.0 mm posterior to bregma; 2.6 mm lateral from midline; 2.0 mm ventral) were performed as described by Garcia-Osta et al. (2006). PREPL antisense oligodeoxynucleotide (ODN) (5′-G*T*T*AGTCGGCCATCGGCA*T*G*C-3′) and scrambled ODN (5′-T*T*C*TCCGAACGTGTCAAT*C*G*T -3′) dissolved in PBS

(2 nmol/μl) were injected bilaterally into the hippocampi 5 hours before LTP recording. Both ODNs were phosphorothioated on the three terminal bases at each end to protect against nuclease degradation. ODNs were reverse phase cartridge purified and purchased from Gene Link (Hawthorne, NY). ODN injections were performed as described previously (Garcia-Osta et al., 2006).

Acyl-Biotin Exchange Assay. Sixty to eighty percent confluent cells in a 10-cm^2 dish were scraped off in 500 μl lysis buffer (LB: 1% IGEPAL, 50 mM Tris-HCl, 150 mM NaCl, 10% glycerol, 1× protease inhibitor cocktail, pH 7.5) and collected in Eppendorf tubes (1.7 ml). The entire experiment was carried out at 4°C on ice unless otherwise stated. Cells were then passed through the insulin syringe (28G) 15–20 times and sonicated for 20 seconds on ice. The lysate was centrifuged at 14,000 rpm at 4°C for 15 minutes. Meanwhile, 2 M N-ethylmaleimide (NEM) stock solution was made fresh in 100% ethanol. After centrifugation, the supernatant was mixed with 2 M NEM stock in another set of prechilled tubes to reach a final NEM concentration of 50 mM. The tubes were briefly vortexed and incubated on a rocker at 4°C overnight. The next day, 1.2 ml cold methanol (at −60°C) was added to each tube followed by incubation on dry ice for 30 minutes. The tubes were then centrifuged at 14,000 rpm at 4°C for 3 minutes. The supernatant was discarded, and the pellet was resuspended in 100 μl solubilization buffer (SB: 4% SDS, 50 mM Tris-HCl, 5 mM EDTA, pH 7.2). The volume was then scaled up to 500 μl with LB, pH 7.2. The lysate was then split equally into two tubes followed by addition of 2 M hydroxylamine solution (HAM solution: 2 M HAM in LB, pH 7.2) to obtain a final HAM concentration of 1 M. Samples were incubated on a rocker for 60 minutes at room temperature. Then the methanol precipitation step was repeated. The pellets were resuspended in 50 μl SB and scaled-up to 250 μl with LB, pH 6.2. Two hundred fifty microliters Biotin-BMCC buffer (10 μM Biotin-BMCC in LB, pH 6.2) was added to each sample to make a final volume of 500 μl. The samples were incubated on a rocker for 60 minutes at 4°C and then processed for western blotting.

Quantification of Sulfhydryl Groups (Ellman's Assay). To evaluate the experimental efficiencies of NEM blocking, HAM depalmitoylation, and biotin-BMCC labeling, 5,5′-dithio-bis-2-nitrobenzoic acid (DTNB, also known as Ellman's reagent) was used to quantify the level of free sulfhydryl groups throughout the acyl-biotin exchange (ABE) palmitoylation assay. Fifteen-microliter samples were saved after NEM incubation, HAM treatment, and Biotin-BMCC labeling. Five-microliter protein samples were added per well in triplicate on 96-well plates. Different buffer systems under the three experimental conditions were also added (5 μl/well) as blank controls. Fifty microliters of Ellman's reagent solution (4 mg/ml DTNB, 0.1 M sodium phosphate pH 8.0, 1 mM EDTA) was added to each well and incubated with protein samples at room temperature for 15 minutes. Absorbance at 412 nm was measured using a Bio-Rad plate reader.

SDS-PAGE Gel Electrophoresis. SDS-PAGE was carried out using the Bio-Rad mini-PROTEAN gel electrophoresis system. Protein samples from N2A, N2A APP, and HT22 cells and corresponding shPREPL cells without or with rescue of PREPL, boiled in Laemmli buffer at 95°C for 5 minutes, were loaded onto 10% gels along with 4-μl protein standards (Bio-Rad Precision Plus Dual Color #161-0374). Sample stacking was carried out at 70 V followed by separation of the protein bands at 120 V until the dye front reached the gel bottom.

Western Blotting. SDS-PAGE protein gels were transferred to nitrocellulose membranes using Bio-Rad Trans-Blot Electrophoresis Transfer System overnight at 25 V, 4°C. Nitrocellulose membranes were blocked for 60 minutes in 5% skimmed milk dissolved in 50% TBS-T (20 mM Tris, 140 mM NaCl, 0.05% Tween 20) and 50% Odyssey Blocking Buffer. The membranes were then incubated with primary antibodies (1:800 dilution in 50% TBS-T and 50% Odyssey Blocking Buffer) for either PREPL, AP-1, calnexin, chromogranin A, SNAP 25, VAMP2, Tau, phospho Tau S491 (pTau S491), phospho Tau S698 (pTau S698), proprotein convertase 1 (PC1), or proprotein convertase 2 (PC2) (Chakraborty et al., 2006) and tubulin (1:5000 as loading control) overnight at 4°C on a rocking shaker. The next day, membranes were washed three times with TBS-T and incubated with anti-mouse or anti-rabbit LI-COR IRDye secondary antibodies at 1:10,000 dilution for 60 minutes at room temperature. After incubation with secondary antibodies, membranes were washed three times with TBS-T and imaged using LI-COR Odyssey Infrared Imaging System. To probe biotinylation in samples after ABE, LI-COR IRDye Streptavidin CW800 (#626-32230) was added at 1:10,000 dilution along with IRDye secondary antibodies for 60 minutes at room temperature before imaging.

Data Analysis and Statistics. Data analysis and graphical illustration were performed using Prism 9.0 software. The P value cutoff used in this study is 0.05. *, **, ***, and **** in the figures refer to $P \leq 0.05$, ≤ 0.01, ≤ 0.001, and ≤ 0.0001 respectively. The statistical analysis and the sample size are described in the figure legends. We considered biologic replicates the measurements of biologically distinct samples. In some experiments, we combined the data from the two PREPL shRNA constructs and added as a biologic replicate. In the graphs, the error bars indicate the standard deviation; each dot represents a biologic replicate.

Results

PREPL Is a Network Driver Downregulated in Human Sporadic LOAD Postmortem Samples. We have previously reported on a large cohort of matched WGS and RNA sequencing (RNA-seq) data from 364 human postmortem brains of late-onset Alzheimer's disease and control subjects from the Mount Sinai Biobank (MSBB) (Wang et al., 2018). These data allowed us to conduct an integrative network analysis to characterize the gene expression changes and critical molecular pathways underlying vulnerability to LOAD at different stages of disease progression. A Bayesian probabilistic causal network (Zhu et al., 2007; Zhang et al., 2013) of gene-gene interaction signaling maps was built by integrating WGS-based expression quantitative trait loci (eQTLs), RNA-seq gene expression, and known transcription factor (TF)-target relationships. In this Bayesian probabilistic causal network, PREPL, downregulated by 30% in demented brains versus control brains (t test, P = 1.1E-7), was identified as a network hub node by using the key driver analysis (Zhang et al., 2013; Zhang and Zhu, 2013; Wang et al., 2021). Genes in the network neighborhood of PREPL were significantly enriched for genes downregulated in the demented brains [fold enrichment (FE) = 4.3, Fisher's exact test (FET) P = 7.4E-6] (Fig. 1A).

PREPL expression showed a negative correlation with a number of cognitive/neuropathological traits, including clinical dementia rating (CDR) scale (Spearman's correlation r = −0.47, P = 6.0E-13) (Fig. 1B), CERAD score (r = −0.41, P = 5.1E-10), Braak score (r = −0.44, P = 4.7E-11), and mean plaque density (r = −0.39, P = 2.9E-9). A similar trend of PREPL expression was noticed in the hippocampus of aged rats in that PREPL mRNA levels decreased in older animals (Supplemental Fig. 1). The disease-associated downregulation of PREPL in inhibitory neurons (0.77-fold, P = 2.8E-17) and astrocytes (0.71-fold, P = 2.9E-3) from brains with LOAD pathology was confirmed using the single-nucleus RNA-seq (snRNA-seq) dataset from the ROSMAP cohort (Mathys et al., 2019). In addition, this snRNA-seq data revealed that PREPL was robustly expressed in neurons at levels higher than other cell types, a pattern consistently observed in separate human brain single-cell RNA-seq data (Darmanis et al., 2015) (Fig. 1C).

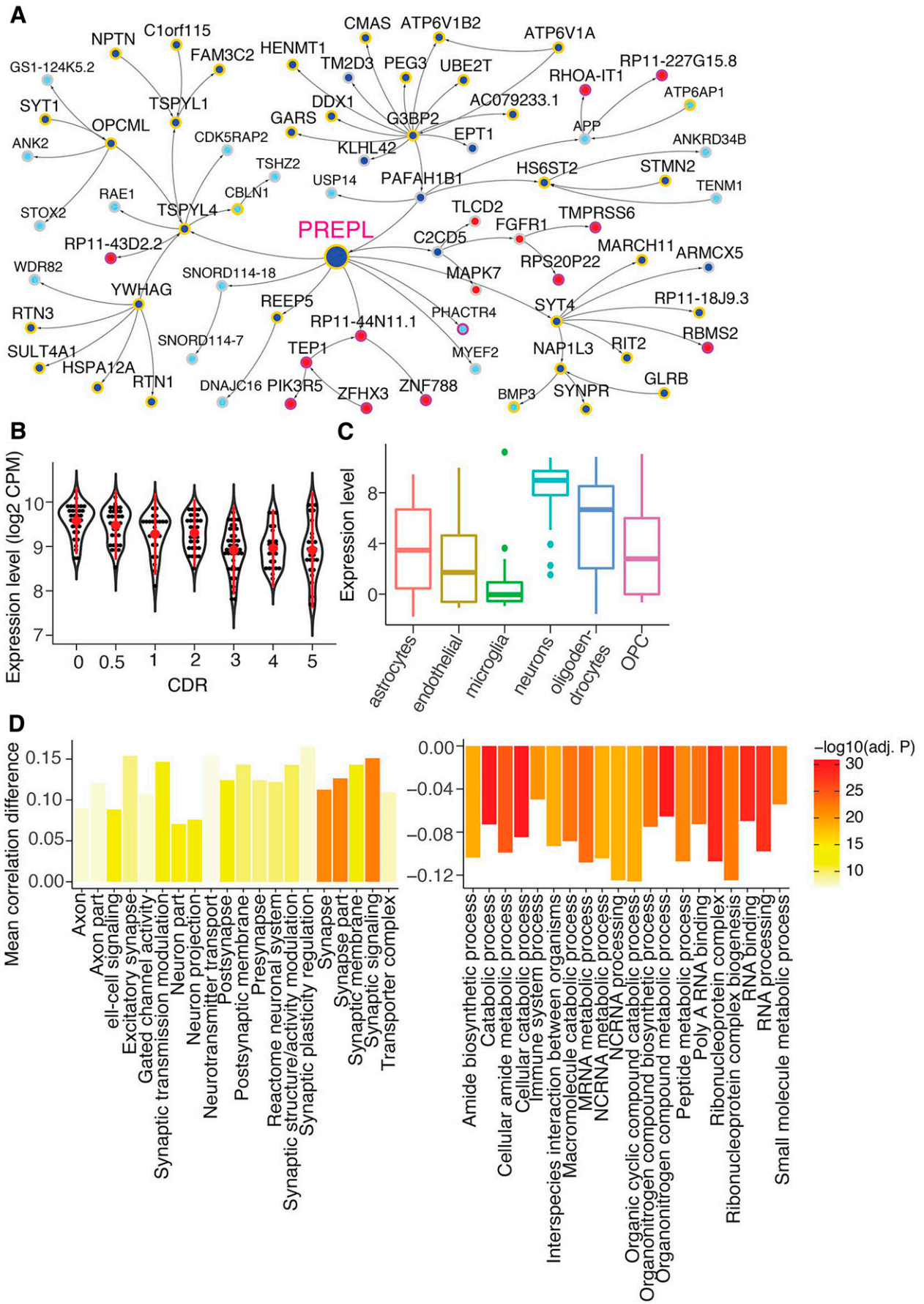

Fig. 1. PREPL is a network key driver downregulated in human sporadic LOAD postmortem samples. (A) Subnetwork around PREPL. Genes differentially expressed in dementia brains are colored in blue (downregulated) or red (upregulated). PREPL is downregulated in AD brains. *(Continued)*

PREPL-Centric Differential Correlation Analysis Reveals Network Reconfiguration in LOAD Brains. To further understand the functional context under which PREPL operates in LOAD, we sought to test if PREPL exhibited a loss or gain of connection with known gene ontology (GO) and canonical pathway genes by Spearman's correlation coefficient analysis. For this purpose, we computed the correlation of gene expression between PREPL and all other genes annotated in the GO/pathway gene sets curated in the MSigDB (v6.1) for dementia (CDR $\geq$1) and nondementia control brains (CDR $<$1) of the MSBB cohort separately (Fig. 1D). Then for each of the 7246 GO/pathway gene sets, we compared the PREPL-centric correlation coefficients (r) of the gene set members between dementia and nondementia control brains using Wilcoxon paired rank sum test. We found that 1645 gene sets showed significant change of correlation with PREPL in dementia versus nondementia brains at a false discovery rate (FDR) $\leq$0.05, a majority (85.6%) of which had loss of correlations. As shown in Fig. 1D, the top MSigDB terms showing loss of correlations with PREPL include metabolic pathways like catabolic process (mean decrease of r = $-$0.07 across pathway members, FDR-adjusted Wilcoxon paired rank sum test P = 1.7E-35) and RNA processing (mean decrease of r = $-$0.1, adjusted P = 1.5E-31). Interestingly, immune system processes showed loss of correlations by an average decreased r of $-$0.05 (adjusted P = 2.3E-21). Among the most significant GO/pathways with gain of correlation are neuronal system related pathways such as synaptic signaling (mean increase of r = 0.15, adjusted P = 6.9E-23), synapse (mean increase of r = 0.11, adjusted P = 3.5E-22), and excitatory synapse (mean increase of r = 0.15, adjusted P = 5.7E-12).

Multiomics Analyses Reveal PREPL As a Modulator of Protein Trafficking and Secretion. To explore how PREPL modulates essential pathways related to AD pathogenesis, we conducted RNA-seq analyses in PREPL knockdown (KD) cells (Fig. 2). For these studies, we used a mouse neuroblastoma cell line, Neuro 2A (N2A), and knockdown of PREPL expression using PREPL shRNA. Knockdown of PREPL was validated by qRT-PCR, imaging, and western blot analysis (Supplemental Fig. 2). RNA-seq data analysis identified 219 upregulated and 206 downregulated genes in PREPL KD cells (Fig. 2A; Supplemental Table 1). PREPL was marginally downregulated with 18% reduction (one-tailed t test; P = 0.027). A GO enrichment analysis for PREPL KD signatures was carried out using the MSigDB gene annotation collections. The enriched GO terms for the downregulated genes are cholesterol biosynthesis, alcohol metabolic process, and sterol metabolic process [up to 41.8-fold enrichment (FE) and FDR-adjusted P = 2.3E-18] (Fig. 2A; Supplemental Table 2). The enriched GO terms for the upregulated genes are multicellular organism signaling, transporter complex and nervous system processes (up to 5.9-FE and FDR-adjusted P = 1.0E-3) (Supplemental Table 2). It is interesting to note that the differentially expressed genes (DEGs) in PREPL KD were enriched for both up- or downregulated genes in human AD brains (Supplemental Table 3).

Next, we investigated the protein level changes using proteomics analyses of PREPL KD by tandem mass spectrometry. In total, 516 upregulated proteins and 528 downregulated proteins were identified (Fig. 2B; Supplemental Table 4). Top GO pathways enriched in the differentially expressed proteins are shown in Fig. 2B, with complete results summarized in Supplemental Table 5. Upregulated proteins were mostly enriched for mitochondrial envelope and organelle inner membrane pathway genes (up to 2.6-FE and FDR = 9.5E-22), whereas downregulated proteins were mostly enriched for the actin filament bundle, actomyosin, and endoplasmic reticulum lumen (up to 3.5-FE, FDR = 5.2E-3). When overlapping with DEGs in human AD brains, we found that only downregulated proteins presented significant enrichment of AD DEGs (Supplemental Table 6).

Comparing the differentially expressed genes with proteins in PREPL KD, we found 35 that were common (Fig. 2C), among which 22 genes were consistent in the direction of change between the two datasets (Fig. 2D).

Finally, the comparison between the top GO pathways enriched in RNA-seq (Supplemental Table 2) and proteomics (Supplemental Table 5) data indicated a downregulation of genes related to cholesterol biosynthesis and an upregulation of proteins related to mitochondria compartment. Also, the upregulated proteins were generally involved in lipid transport, steroid biosynthesis, and lipid catabolic processes. These results suggest a role for PREPL in lipid metabolism that could result in modulating protein processing, trafficking, and secretion.

PREPL Knockdown Impairs Cell Proliferation and Survival. Next, we performed cellular studies to gain an insight into the mechanisms of action of PREPL, and three different cell models were used for this: 1) N2A, 2) N2A APP, and 3) a mouse hippocampal cell line (HT22), generating PREPL KD with each (Supplemental Fig. 2).

One of the first observations from culturing PREPL KD cells was the impairment in cell growth (Supplemental Fig. 3). To confirm this observation, we measured the growth of viable cells in control and PREPL KD cells at different time points. Cells with PREPL KD exhibited slower growth, and at 72 hours there were 40%–60% fewer viable cells in both N2A and HT22 PREPL KD cells compared with control (Supplemental Fig. 3, A and C). Similar results were seen for N2A APP cells—after 72 hours, the number of viable cells was 80% fewer with PREPL KD compared with control (Supplemental Fig. 3B, left panel). In a clonogenic assay, N2A PREPL KD cells exhibited an 80% decrease in colony-forming units (Supplemental Fig. 3A, right panel). It should be noted that the number of nonviable cells was not increased in N2A APP PREPL KD cells (Supplemental Fig. 3B, right panel), suggesting that the reduction in cell proliferation and survival is not related to an increase in cell death. To confirm that changes in cell proliferation were directly connected to the knockdown of PREPL expression, we overexpressed wild-type

(B) Violin and dot plot showing the distribution of PREPL expression stratified by CDR. The red dot in the middle is the median value, and the red line in the center represents the interquartile range of the density estimate. There is a significant negative correlation between PREPL expression and CDR (Spearman's r = $-$0.47, P = 6.0E-13). (C) Brain cell type–specific expression of PREPL based on single-cell RNA-seq data from (Darmanis et al., 2015). (D) Top gene ontology (GO) and pathways showing increased (left) or decreased (right) correlation with PREPL in dementia brains. Y-axis denotes the mean difference of correlation coefficients between dementia and nondementia brains. Color intensity denotes adjusted Wilcoxon paired rank sum test P value.

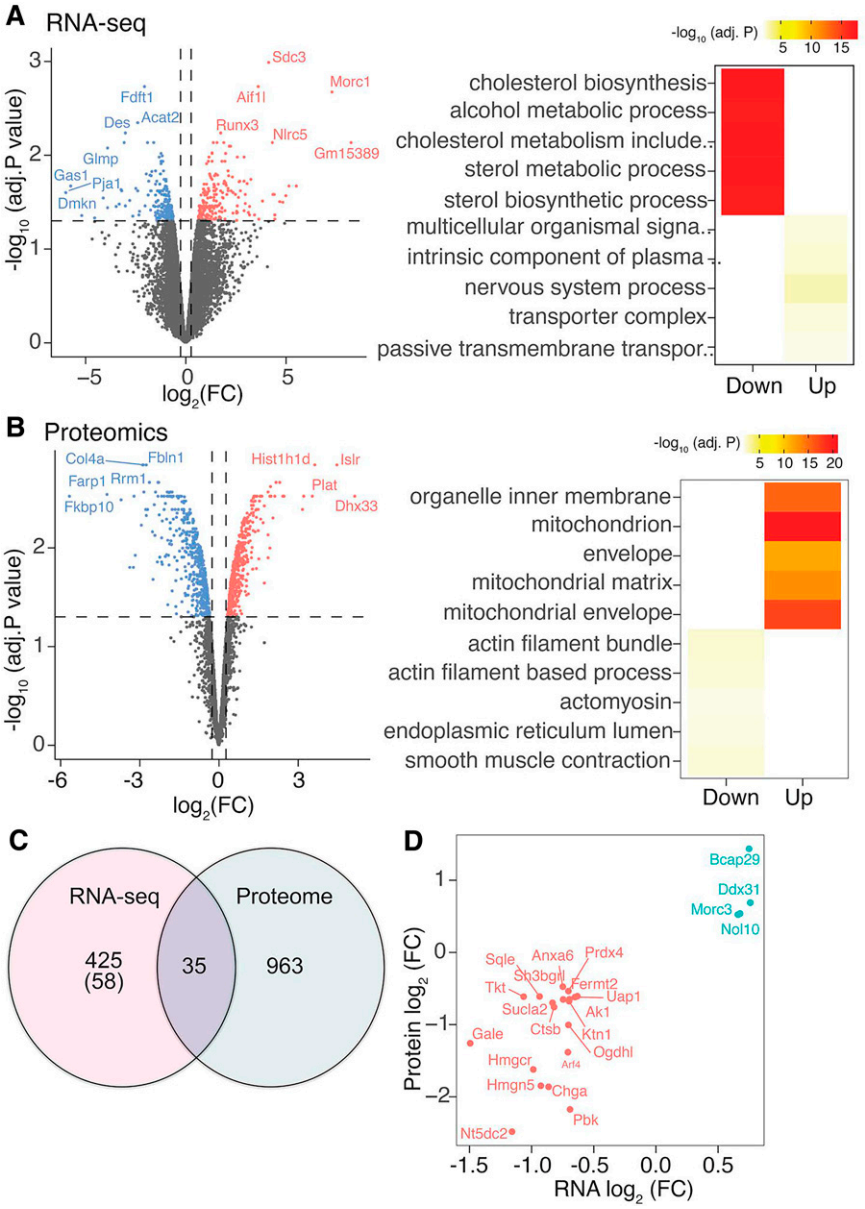

Fig. 2. RNA-seq and proteomics analyses reveal RNA and protein signatures induced by PREPL KD. (A) Volcano plot showing the differential gene expression induced by PREPL KD in N2A cells using RNA-seq. Right panel shows top gene ontology pathways enriched in the differentially expressed genes caused by PREPL KD. (B) Volcano plot showing the differential protein expression induced by PREPL KD using proteomics. Right panel shows top gene ontology pathways enriched in the differentially expressed proteins caused by PREPL KD. (C) Overlap between RNA and protein signatures caused by PREPL KD. Although there are 425 DEGs by RNA-seq, only 93 (= 58 + 35) are present in the proteomics data. (D) Scatter plot showing the log2 fold change (FC) of the differentially expressed genes that present consistent direction of change in both RNA-seq and proteomics.

PREPL in HT22 control and PREPL KD cells. PREPL overexpression rescued the decrease in cell proliferation seen due to knockdown (Supplemental Fig. 3C, middle panel). Next, we investigated the influence of extracellular components on cell proliferation. Conditioned media from HT22 control cells was supplemented into PREPL KD cells; this led to a partial rescue of cell proliferation in PREPL KD cells (Supplemental Fig. 3C, right panel). Overall, the results suggest that PREPL modulates cell proliferation by a mechanism that could be related to changes in the contents of the extracellular milieu.

PREPL Modulates Cell Morphology and AP-1 Levels. A previous study, using mouse embryonic fibroblast cell lines, identified an interaction between PREPL and AP-1, a protein that mediates clathrin-coated transport vesicle formation and protein sorting between the trans-Golgi network and endosomes (Wu et al., 2003); this led to the suggestion that PREPL downregulation could lead to disruption of protein trafficking compartments (Morawski et al., 2013; Radhakrishnan et al., 2013). To explore this in our system, we first compared the morphology of wild-type N2A (N2A) and N2A-PREPL KD (PREPL KD) cells. Phase-contrast microscopy shows PREPL KD cells to be larger in size compared with wild-type cells (Fig. 3A). Images obtained using bright-field microscopy (Fig. 3A) and fluorescence microscopy using CellBrite red cytoplasmic membrane dye indicate that PREPL KD causes morphologic alterations in the vesicular compartments, with an increase of vesicle-like structures compared with the N2A cells (Fig. 3C).

Next, we examined the effect of PREPL KD on the levels of AP-1, a trans-Golgi network and endosome marker (Wu et al., 2003) (Fig. 3B). Quantification of single-cell imaging data (using high-throughput microscopy) shows significant increases in AP-1 staining in N2A PREPL KD cells (Fig. 3D, right panel). Western blot analysis of N2A, N2A APP, and HT22 cells and corresponding PREPL KD cells also shows increased AP-1 protein levels in PREPL KD cells (Fig. 3D;

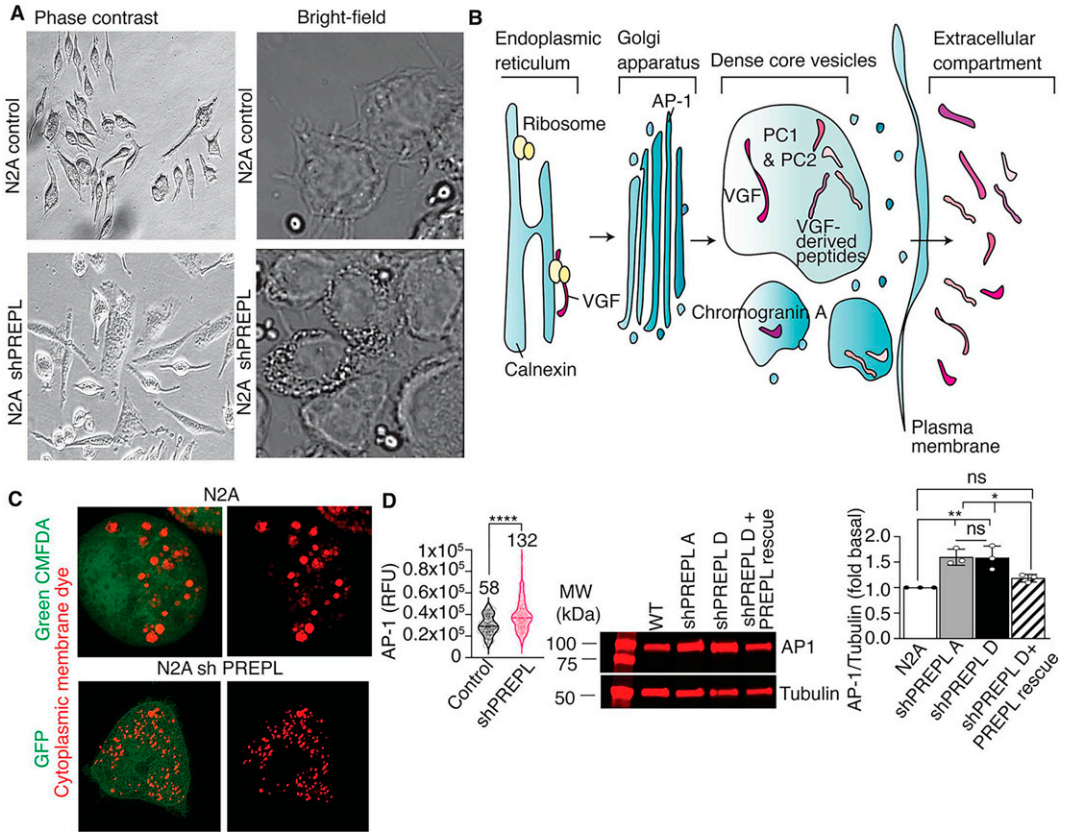

Fig. 3. PREPL modulates the distribution of dense-core vesicle structures, increasing the distribution of adaptor protein-1 (AP-1). (A, left panels) N2A cells and cells with PREPL knockdown grown in 10 cm^2 dishes were imaged as described in *Materials and Methods*. Representative image shows that PREPL knockdown alters the morphology of N2A cells. (A, right panels) Representative bright-field microscopy images at 40× magnification showing changes in the vesicle compartment of N2A shPREPL compared with N2A control cells. (B) Schematic of subcellular compartments and proteins related to protein processing and secretion. (C) Representative confocal microscopy images (100×) of live N2A (labeled with green CMFDA dye) and of N2A shPREPL (expressing GFP fluorescence) cells, where intracellular membranes were labeled with a cytoplasmic membrane dye (red), show that PREPL knockdown alters the size and number of intracellular vesicles. (D, left panel) Distribution of AP-1 in N2A control and N2A shPREPL cells using high throughput microscopy. Each dot represents a counted cell. Welch's t test, $^{****}P < 0.0001$. (D, middle and right panels) Representative western blot (original in Supplemental Fig. 4) and quantification showing that two different shPREPL constructs (shPREPL A and shPREPL D) cause an increase in AP-1 protein levels and that PREPL expression in knockdown cells rescues wild-type phenotype. One-way ANOVA with Tukey's multiple comparison test; $^{*}P < 0.05$, $^{**}P < 0.01$, ns = not significant.

Supplemental Fig. 4A). Interestingly, we find that PREPL rescue in the PREPL KD cells leads to restoration of AP-1 to levels similar to the control cells (Fig. 3D; Supplemental Fig. 4A). These results suggest an association between PREPL deficiency and Golgi dysfunctions as well as a potential role of PREPL in the AP-1–mediated protein trafficking.

PREPL Regulates Protein Processing and Secretion. We examined the effect of PREPL KD on components of the regulated pathway of secretion; for this, we selected proprotein convertase 1 and 2 (PC1 and PC2), enzymes involved in protein processing, and also examined the levels of a secreted neuropeptide (VGF-derived peptide AQEE) (Fig. 3B). Using western blot analysis and enzyme-linked immunosorbent assay (ELISA) for AQEE, we find that PREPL KD leads to a significant decrease in the levels of neuropeptide processing enzymes and the VGF-derived peptide AQEE (Fig. 4; Supplemental Fig. 4, B and C). PREPL rescue in the PREPL KD cells leads to restoration of PC1 and PC2 to levels similar to those seen in control cells (Fig. 4; Supplemental Fig. 4, B and C). Next, we investigated if the reduction in peptide processing activity affected secretion of AQEE under stimulated and nonstimulated experimental conditions. As expected, the levels of secreted AQEE were augmented in controls after exposure to the depolarizing buffer (Fig. 4E). However, PREPL KD cells exhibited a lower level of secreted AQEE under both depolarizing and nondepolarizing conditions (Fig. 4E). Together, our results demonstrate that PREPL plays a role in modulating the secretory pathway that regulates protein exocytosis.

G-Protein–Coupled Receptors Have Differential Dynamics of Internalization in PREPL KD Cells. To explore if PREPL plays a role in protein endocytosis, we examined the kinetics of G-protein–coupled receptor (GPCR) internalization. GPCRs, upon receptor activation, are known to be internalized and transported to endosomal compartments, followed by either degradation or recycling to cell surface (Eichel and von Zastrow, 2018). The dynamic processes of receptor internalization and recycling are also dependent on the different members of the adaptor protein family and clathrin-coated vesicles (von Zastrow and Sorkin, 2021).

To investigate the effect of PREPL KD on the endocytic mechanism, we treated N2A and N2A PREPL KD cells with deltorphin II, a classic delta opioid receptor (DOR) agonist, or with HU210, a potent cannabinoid receptor (CB_1R) agonist. The level of internalized GPCRs was assessed by ELISA

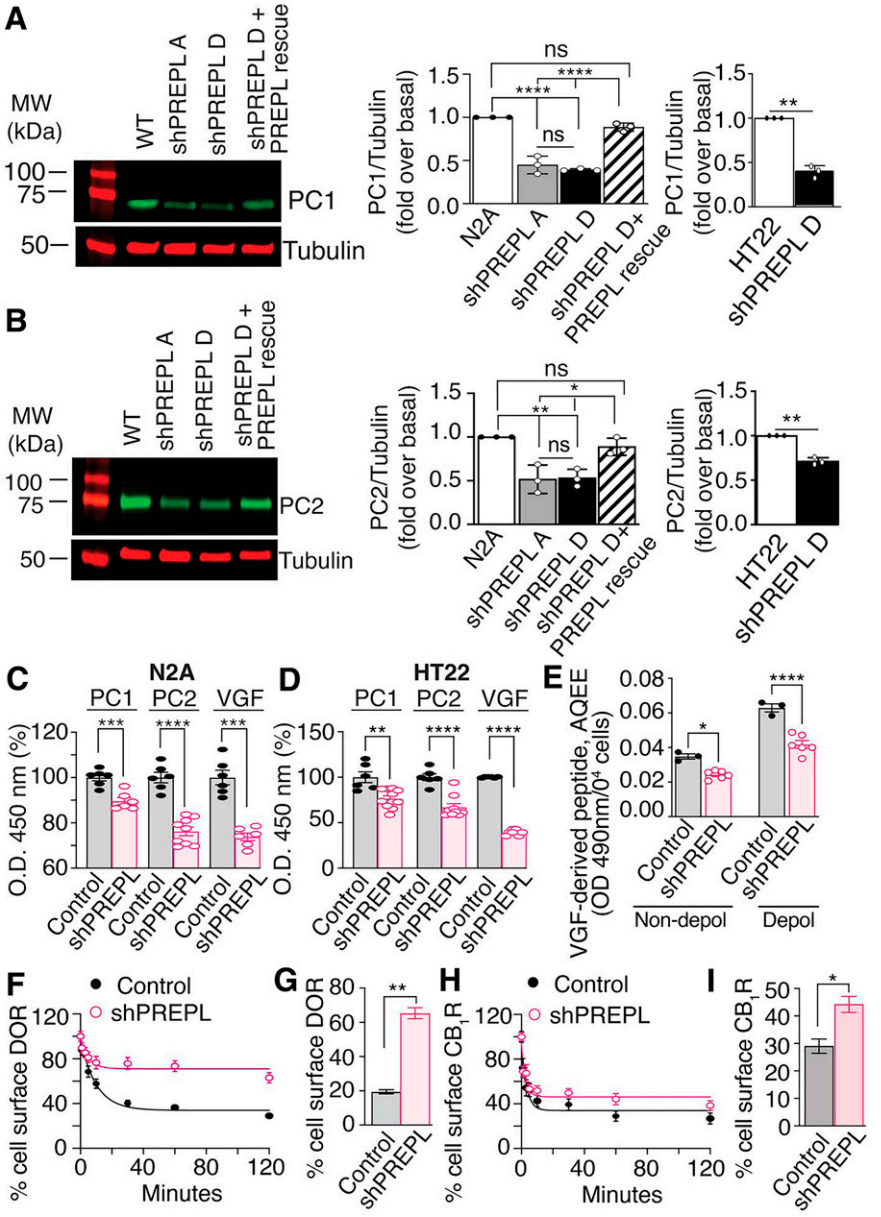

Fig. 4. PREPL knockdown downregulates proteins related to protein processing and secretion and modulates agonist-induced G-protein–coupled receptor endocytosis. (A and B) Representative western blots (originals in Supplemental Fig. 4) and quantification showing that two different shPREPL constructs (shPREPL A and shPREPL D) cause a decrease in PC1 (A) and PC2 (A) levels in N2A and HT22 cells and that PREPL expression in knockdown cells rescues wild-type phenotype. One-way ANOVA with Tukey's multiple comparison test; $*P < 0.05$, $**P < 0.01$, $****P < 0.0001$, ns = not significant. (C and D) Whole-cell ELISA showing that knockdown of PREPL (shPREPL) in either N2A (C) or HT22 (D) cells decreases the levels of PC1, PC2, and VGF-derived peptide AQEE. Welch's t test; $**P < 0.01$, $***P < 0.001$, $****P < 0.0001$. (E) Levels of the secreted VGF-derived peptide AQEE were measured by ELISA using N2A APP control and N2A APP shPREPL cells under depolarizing (Depol) and nondepolarizing (non-depol) conditions. Each dot represents a biologic replicate. Welch's t test; $*P < 0.05$, $****P < 0.0001$. (F and G) The internalization of the delta opioid receptor (DOR) (F and G) was measured by ELISA using N2A wild-type and N2A shPREPL cells treated with 1 μM deltorphin II (for DOR) for 0–120 minutes. (G) Percentage of cell surface receptors after 2-hour treatment with deltorphin II is shown. (H and I) The internalization of the CB_1 cannabinoid receptor (CB_1R) was measured by ELISA using HT22 wild-type and HT22 shPREPL cells treated with 100 nM of HU210 for 0–120 minutes. (I) Percentage of cell surface receptors after 1-hour treatment with HU210 is shown. Data represent mean ± S.D. ($n = 3$). Two-way ANOVA was used to compare the cell surface receptor expression between control and PREPL KD cells at different time points; $*P < 0.05$, $**P < 0.005$.

(Fig. 4, F–I). DOR internalization could be detected after 10 minutes of treatment with the agonist in control cells (Fig. 4F) and was reduced in PREPL KD cells since even after 60 minutes of agonist exposure, the level of DOR at the membrane was significantly higher in PREPL KD cells (60% of DOR at the cell surface) compared with control cells (20% of DOR at the cell surface) (Fig. 4G). Similar observations were made with CB_1R (Fig. 4, H and I). These results support the idea that PREPL plays a role in protein trafficking.

PREPL Modulates Levels of Intracellular Vesicles/Compartments. Since our studies suggest the involvement of PREPL with pathways related to protein processing, secretion, and receptor trafficking, we examined the effect of PREPL knockdown on levels of a number of proteins associated with intracellular vesicles: 1) calnexin, an endoplasmic reticulum marker; 2) chromogranin A (CgA), a secreted protein that can serve as a marker for dense core vesicles; and 3) vesicle-associated membrane protein 2 (VAMP2) and synaptosomal-associated protein 25 (SNAP25), proteins responsible for mediating fusion of synaptic vesicles for neurotransmitters release (Fig. 3B). Single cell imaging and western blot analysis detect decreases in the levels of calnexin, CgA, and VAMP2 and increases in SNAP25 levels in PREPL KD cells (Fig. 5; Supplemental Fig. 5). These results are consistent with those of proteomics analyses that found members of the SNARE family to be downregulated in PREPL KD cells (Fig. 2). The decreased expression of chromogranin A, a protein associated with Aβ accumulation (Lechner et al., 2004; Mattsson et al., 2010), also correlates with the decrease seen in the multiomics analysis of PREPL KD cells (Fig. 2). We also find that PREPL rescue in the PREPL KD cells leads to restoration of calnexin, chromogranin A, SNAP25, and VAMP2 to levels similar to those in control cells (Fig. 5; Supplemental Fig. 5).

Next, to assess the localization of PREPL with various endosomal compartments in N2A cells by confocal microscopy, we used the following markers of endosomal compartments:

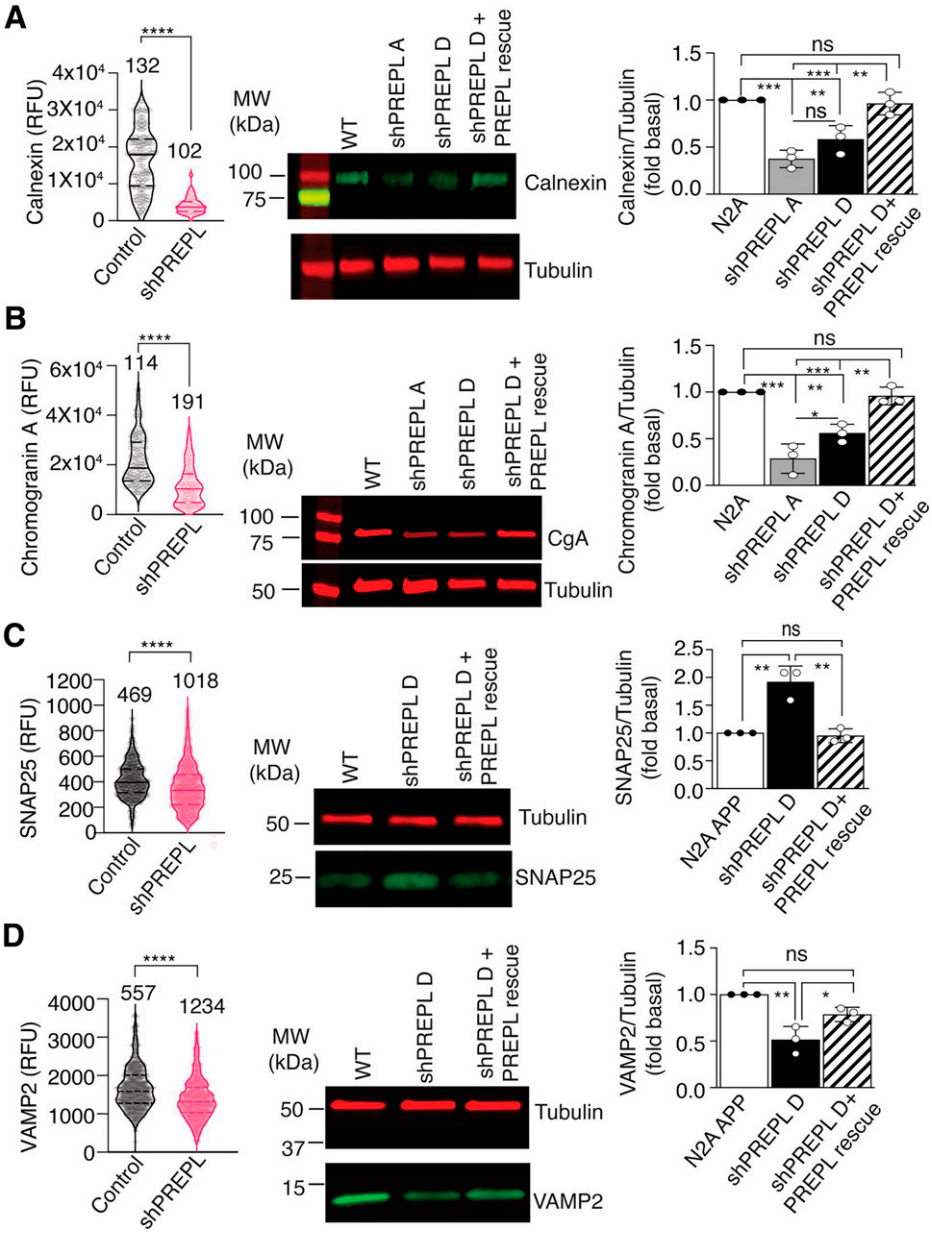

Fig. 5. PREPL modulates the levels of calnexin, chromogranin A, SNAP25, and VAMP2. Levels of calnexin (A), chromogranin A (CgA) (B), SNAP25 (C), and VAMP2 (D), were determined by high-throughput microscopy (quantitation on left panels) or by western blot analysis (middle and right panels) as described in *Materials and Methods* using either N2A (N2A APP for microscopy analysis of SNAP25 and VAMP2) or shPREPL knockdown cells. In the volcano plot, each dot represents a counted cell, and the dashed lines represent the mean and standard error. Welch's t test; $^{****}P < 0.0001$. For westerns, a representative blot (original in Supplemental Fig. 5) is shown (middle panels). (Right panels) Quantification showing that two different shPREPL constructs (shPREPL A and shPREPL D) cause a decrease in calnexin, CgA, and VAMP2 and an increase in SNAP25 protein levels; PREPL expression in knockdown cells rescues wild-type phenotype. One-way ANOVA with Tukey's multiple comparison test; $^{*}P < 0.05$, $^{**}P < 0.01$, $^{***}P < 0.001$, ns = not significant.

Rab 5 for early endosomes, Rab 7 for late endosomes to lysosome transport, Rab 9 for late endosome to TGN transport, TGN38 for Golgi, and calnexin for ER. We found that PREPL exhibits colocalization with all of these markers, albeit to different extents (Supplemental Fig. 6). Interestingly, comparison of staining for these vesicular markers between N2A and N2A with PREPL KD cells shows increased numbers and/or density of these vesicles in PREPL KD cells (Supplemental Fig. 6). Together, these results support the idea that PREPL regulates vesicular trafficking.

PREPL Modulates Cellular Hallmarks of AD. Next, we assessed the levels of extracellular amyloid beta-42 (Aβ42) and extent of Tau phosphorylation to investigate if changes in PREPL expression affect these cellular hallmarks of AD (Fig. 6).

The accumulation of Aβ peptides, particularly Aβ42 (42 amino acid length), is known to be an early trigger for AD pathogenesis (Selkoe and Hardy, 2016). Analysis of extracellular levels of Aβ42 by ELISA (using conditioned media from N2A APP and PREPL KD cells) detected elevated levels of Aβ42 peptides in PREPL KD cells compared with controls (Fig. 6A). Next, we examined Tau phosphorylation using phospho-specific antibodies to various phospho-sites on Tau since phosphorylation of Tau at specific residues has been reported to affect its interaction with microtubules and induce neurofibrillary tangles (NFLs) (Augustinack et al., 2002; Foidl and Humpel, 2018). First, we validated the phospho-specific Tau antibodies that were generated using a yeast-display technology (Lemos Duarte et al., 2021). Quantitation of single-cell imaging of N2A cells with Tau KD shows a decrease in the fluorescence staining with all of the antibodies tested (Supplemental Fig. 7). Of interest is the staining of PREPL KD cells with phospho-specific antibodies against the residues S491, S554, and S698 of mouse PNS-Tau isoform. These epitopes have 100% identity to human Tau and correspond respectively to S199, S262, and S396 of human 2N4R

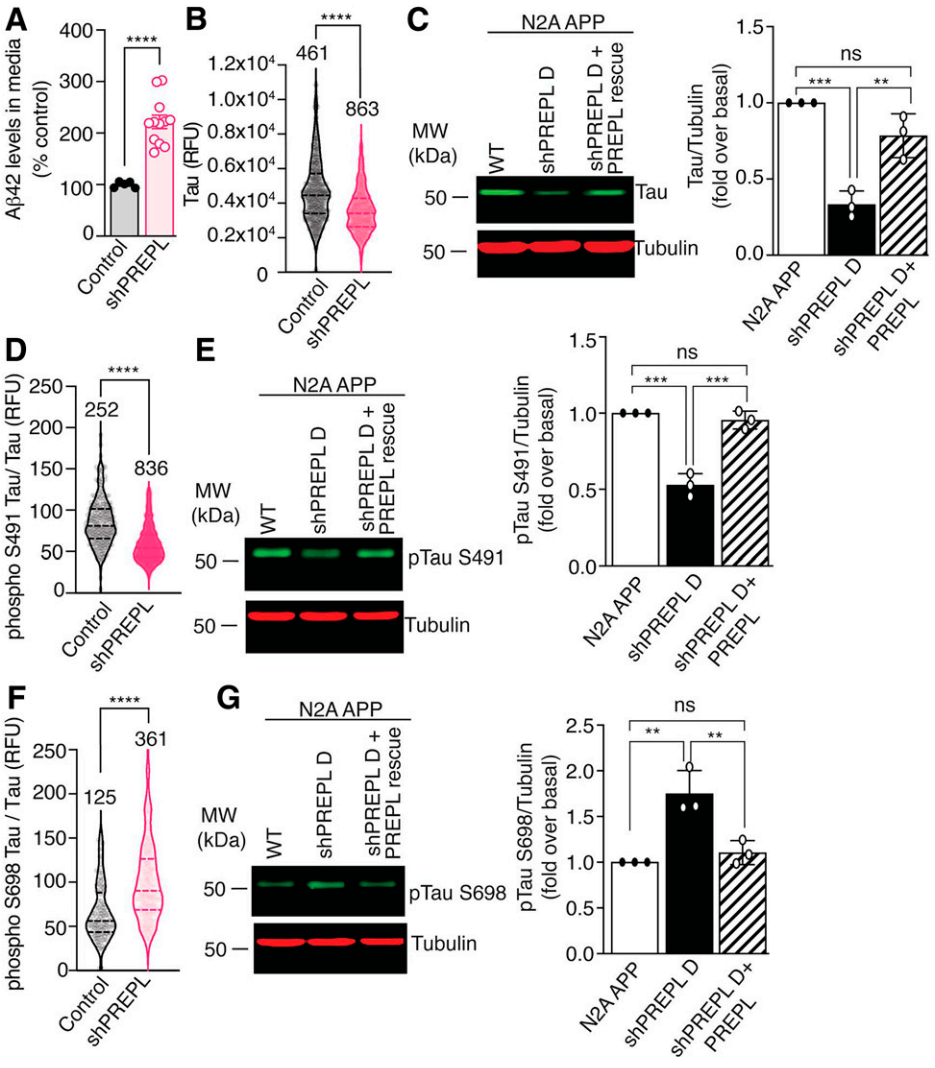

Fig. 6. PREPL modulates important hallmarks of AD in N2A APP cells. (A) ELISA measuring extracellular levels of Aβ42 peptides. Each dot represents a counted cell. Welch's t test; $^{****}P < 0.0001$. (B, D, and F) Quantitation of Tau phosphorylation measured by high-throughput microscopy analysis using antibodies against specific phosphorylated Tau residues. Cell Profiler was used to quantitate the fluorescence intensity. The levels of phosphorylation were normalized by dividing the fluorescence intensity measurements for each cell with the mean fluorescence intensity of total Tau. Each dot represents a counted cell; cell numbers are shown in the graph. Welch's t test; $^{****}P < 0.0001$. (C, E, and G) A representative blot (original in Supplemental Fig. 7) for Tau, phospho TauS491 (pTau S491), and phospho TauS698 (pTau S698) is shown (middle panels). (Right panels) Quantification showing that two different shPREPL constructs (shPREPL A and shPREPL D) cause a decrease in Tau and pTau S491 and an increase in pTau S698 protein levels; PREPL expression in knockdown cells rescues wild-type phenotype. One-way ANOVA with Tukey's multiple comparison test; $^{**}P < 0.01$, $^{***}P < 0.001$, ns = not significant.

isoforms. Initially, we noticed a reduction in the expression of total Tau in PREPL KD (Fig. 6B). However, comparison of the ratio of Tau phosphorylation to total Tau suggests that PREPL can differentially modulate Tau phosphorylation at specific residues. More specifically, we noticed a decrease in phosphorylation levels at residues S491 and S554 and an increase in the phosphorylation of the residue S698 in PREPL KD cells (Fig. 6; Supplemental Fig. 7). Decreases in Tau and phospho Tau S491 and increases in phospho Tau S698 levels in PREPL KD cells were confirmed by western blot analysis. Finally, PREPL rescue in these cells leads to restoration of the signal to levels similar to those seen in control cells (Fig. 6; Supplemental Fig. 7).

PREPL Modulates Long-Term Potentiation in Hippocampus. To determine the role of PREPL in hippocampal synaptic transmission, we used field electrophysiology (Fig. 7). For these studies, PREPL was knocked down using antisense oligodeoxynucleotides (ODNs). We tested three different ODN constructs and selected the construct 5′G*T*T*AGTCGGCCAT CGGCA*T*G*C-3 (named ODN3) that was found to reduce PREPL expression by 70% (Supplemental Fig. 8).

To assess whether PREPL expression impacts presynaptic function, we first estimated the probability of release (Pr) by analyzing paired-pulse facilitation (PPF), a form of short-term synaptic plasticity. This form of short-term synaptic plasticity is determined, at least in part, by changes in probability of presynaptic neurotransmitter release (Zucker and Regehr, 2002). We found that PPF in mice with PREPL KD was not different from control mice (injected with oligos) (Fig. 7B), which rules out effects on presynaptic function.

Next, we investigated the effects of PREPL KD on hippocampal long-term potentiation (LTP). After inducing the CA3-CA1 LTP, we observed an LTP deficit in PREPL-ODN–injected mice compared with scrambled-ODN–injected mice (Fig. 7C). Since impairment in hippocampal LTP has been described as a cellular/molecular correlate of memory (Nalbantoglu et al., 1997; Gelman et al., 2018) and loss of memory is a hallmark of AD, our results support the notion that PREPL plays a role in modulating synaptic plasticity.

PREPL Role in Modulating Protein Palmitoylation Process. A recent study reported PREPL to have a (thio)esterase activity and function as a depalmitoylating enzyme (Rosier et al., 2021). As one of the key posttranslational modifications for protein trafficking, protein palmitoylation involves the addition of 16-carbon palmitoyl acid to the free thiol groups of the cysteine residues in proteins (Linder and Deschenes, 2007). Since, PREPL KD affects metabolic proteins related to lipid synthesis and degradation (Fig. 2) we assessed the potential

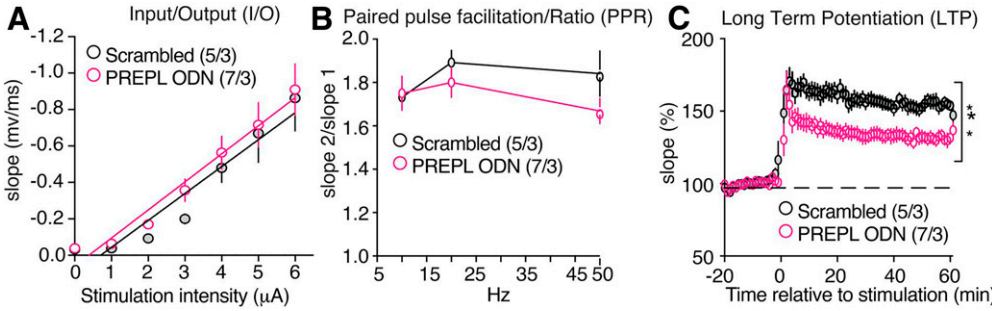

Fig. 7. PREPL modulates long-term potentiation in hippocampus. Basal synaptic transmission and synaptic plasticity in CA1 after PREPL ODN administration. C57BL6 mice were injected bilaterally in the hippocampi with scrambled ODN (Scr ODN, 5′-T*T*T*C*TCCGAACGTGTCAAT*C*G*T-3′) or PREPL ODN (5′-G*T*T*AGTCGGCCATCGGCA*T*G*C-3′), sacrificed after 5 hours, and hippocampal slices used for electrophysiological recordings. (A) Basal synaptic transmission. (B) Paired-pulse facilitation (PPR). (C) Long-term potentiation (LTP). LTP induced by theta-burst stimulation (four pulses at 100 Hz repeated with 10-millisecond interburst intervals) is significantly impaired in PREPL ODN mice (three male mice, five slices, t test, $P < 0.001$).

role of PREPL in protein palmitoylation in N2A cells using the acyl-biotin exchange protocol (Brigidi and Bamji, 2013; Edmonds et al., 2017) (Fig. 8, A–C). Comparison of the levels of palmitoylated proteins in wild-type cells with PREPL KD cells (Fig. 8, D and E) shows that there is an increase in the intensity of biotinylated protein in PREPL KD cells (Fig. 8E). These results are consistent with an overall increase of total protein palmitoylation in PREPL-deficient cells, supporting the potential involvement of PREPL in protein depalmitoylation. Next, we directly examined this using palmostatin M, an acyl protein thioesterase inhibitor reported to block PREPL activity (Rosier et al., 2021). We find that palmostatin M treatment reduces cell viability and more importantly GPCR endocytosis (Figs. 4 and 8; Supplemental Fig. 3) to a manner similar to

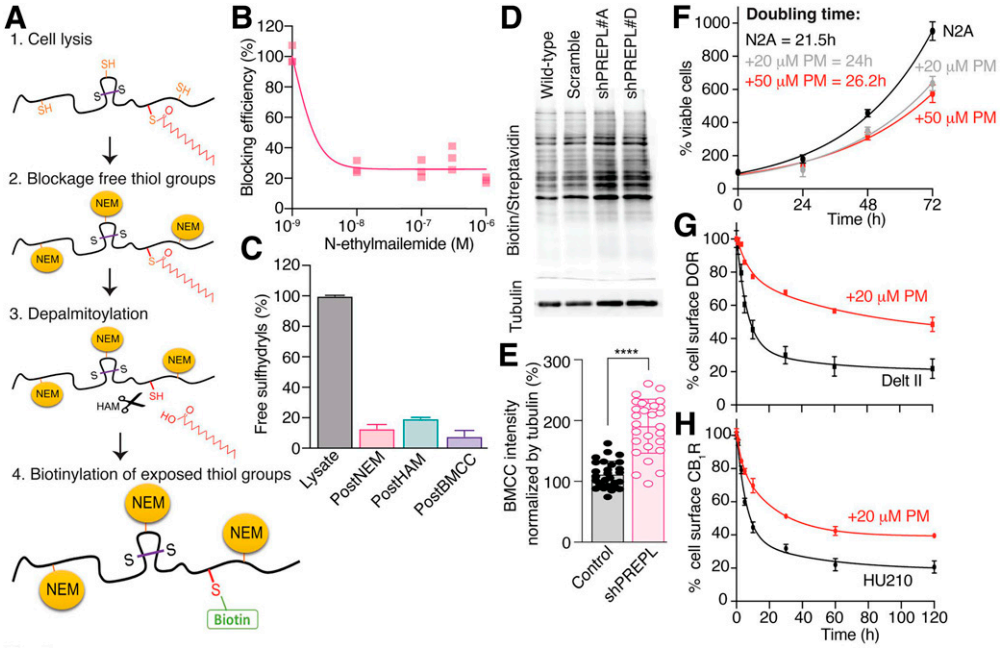

Fig. 8. PREPL knockdown increases total levels of palmitoylated proteins. (A) Schematic representation of the ABE protocol steps. The free thiol groups from the total protein lysate were blocked with N-ethylmaleimide (NEM). Next, the palmitoyl groups were cleaved using hydroxylamine (HAM). After depalmitoylation, the remaining thiol groups were biotinylated. Lysates containing the palmitoylated proteins tagged with biotin were subjected to SDS-PAGE followed by transfer to nitrocellulose membranes. Membranes were stained with biotin/streptavidin, and band intensities were quantified using ImageJ. (B) Using Ellman's reagent, the percentage of free thiol groups was quantified after treatment with different concentrations of NEM for 16 hours at 4°C. (C) The percentage of free thiol groups after each step of the ABE protocol, using Ellman's reagent. (D) The biotinylation of palmitoylated thiol groups was probed with streptavidin IRDye 800CW. Representative blot of two independent experiments. As a loading control, the blot was probed with tubulin. (E) Band intensities of biotinylated proteins were measured by densitometry in different regions of interests (ROIs) using ImageJ. The measurements were made at all of the different molecular weights. Each dot represents an individual densitometry measurement of bands in a selected ROI. The biotin intensities were normalized to endogenous control. Data are the mean of two independent experiments with two different shPREPL constructs. Welch's t test; ****$P < 0.0001$. (F) N2A cell proliferation rates were obtained by measuring the number of viable cells at different time points (0–72 hours) in the absence or presence of palmostatin M (20 and 50 μM) as described in *Materials and Methods*. (G) DOR internalization was measured by ELISA using N2A cells treated with 1 μM deltorphin II for 0–120 minutes in the absence or presence of palmostatin M (20 μM) as described in *Materials and Methods*. (H) CB_1R internalization was measured by ELISA using N2A cells treated with 100 nM of HU210 for 0–120 minutes in the absence or presence of palmostatin M (20 μM) as described in *Materials and Methods*. Data (G and H) represent mean ± S.D. ($n = 3$).

what was observed with PREPL KD cells. Together, these data support a role for PREPL in protein palmitoylation confirming a depalmitoylating activity for PREPL.

Discussion

PREPL deficiency has been associated with hypotonia-cystinuria syndrome in humans (Régal et al., 2014, 2018), an autosomal recessive genetic disease caused by microdeletions of SLC3A1 and PREPL at chromosome 2p21 (Jaeken et al., 2006). Further studies of subjects with isolated PREPL deficiency revealed growth hormone deficiency (Régal et al., 2018; Sayol-Torres et al., 2021) and moderate intellectual disability (Silva et al., 2018; Yang et al., 2020). Furthermore, it was noted that biallelic PREPL mutations alone (without involvement of other genes) can cause intellectual disability (Silva et al., 2018). Together, this led to the hypothesis that PREPL is involved in learning, memory, and cognition. PREPL deficiency has also been associated with AD (Morawski et al., 2013; Zhang et al., 2013; Zhang and Zhu, 2013; Beckmann et al., 2020; Wang et al., 2021). PREPL expression was found to be decreased in the pyramidal layer V of the cortex of AD patients' brains (Morawski et al., 2013). Moreover, PREPL was found to be a potential key network driver downregulated in LOAD (Fig. 1). In this study, we identify and characterize PREPL as a new potential regulator of AD pathogenesis. We find impairment in cellular memory (long-term potentiation) by PREPL knockdown in mouse hippocampus, consistent with the idea that PREPL contributes to learning and memory by affecting synaptic transmission.

An observation of our study is that paired pulse ratio is not affected by knockdown of PREPL, which would appear to contradict observations made by others demonstrating that PREPL plays a role in vesicle secretory functions (Morawski et al., 2013; Radhakrishnan et al., 2013). A potential reason for this could be that PREPL affects a distinct pool of vesicles. There are two different pools of vesicles in the presynaptic terminal, small synaptic vesicles that carry fast-acting neurotransmitters such as glutamate, GABA, acetylcholine, and glycine as well as dense core vesicles that contain larger neuropeptide transmitters and hormones (Park and Kim, 2009). There are also differences in the strength of stimuli needed to release the contents of these vesicles (Park and Kim, 2009). Releasing the content of dense core vesicles requires repetitive sustained stimuli, whereas for small synaptic vesicles a shorter duration of activity such as a single action potential is needed (Park and Kim, 2009). In our paired pulse ratio experiments, only a brief stimulation was applied to the brain slice; this is not enough to induce a release of the dense core vesicle contents. Thus, the lack of differences in paired pulse ratio suggests that PREPL may not be involved in the release of small synaptic vesicles (which release the chemical neurotransmitters) to the same extent as dense core vesicles. In addition, when measuring paired pulse ratio, we are measuring the actions of the excitatory neurotransmission due to glutamate release; therefore, our readout may not be capturing a functional release of dense core vesicles.

Previous studies characterized the interaction between PREPL and adaptor protein AP-1, suggesting a role for PREPL in intracellular protein trafficking (Morawski et al., 2013; Radhakrishnan et al., 2013). We and others have found that PREPL is localized to vesicular compartments and that its expression regulates the expression and function of proteins involved in protein exocytosis, endocytosis, and secretion (Figs. 3–5; Supplemental Figs. 4–6). Of particular interest is the regulation of secretion of neuropeptides such as VGF-derived peptides (Fig. 4). VGF is a neuropeptide precursor, known to be processed to several peptides, that is responsible for modulation of physio/pathologic functions such as spatial memory. In brain tissues and CSF samples from AD patients, VGF levels are consistently decreased (Quinn et al., 2021). In 5× FAD mice, overexpression of VGF partially rescued beta-amyloid–mediated memory impairment and neuropathology (Beckmann et al., 2020). Thus, it is likely that decreased VGF-peptide levels, in combination with decreased expression of vesicle-associated proteins under conditions of decreased expression of PREPL, could contribute, at least in part, to the AD pathogenesis (Park et al., 2020).

In this study, we also found increases in Tau phosphorylation at select sites in cells with decreased expression of PREPL. It has been suggested that although phosphorylation at S^{262} of human Tau (corresponding to S^{554} mouse TAU) is important to Tau interaction with microtubules, it may not contribute to the initial steps of NFT formation (Biernat et al., 1993; Cabrales Fontela et al., 2017). Interestingly, phosphorylation of S^{199} (corresponding to S^{491} mouse Tau) leads to changes in Tau conformation, which further triggers the sequestering of other Tau molecules (Augustinack et al., 2002). Moreover, phosphorylation of S^{396} of 2N4R (corresponding to S^{698} mouse Tau) was mainly found in NFTs, with a strong association with plaque formation (Alonso et al., 2004; Foidl and Humpel, 2018). Here we show that PREPL expression can modulate Tau phosphorylation, a crucial step for NFT formation, at specific residues. Further studies need to characterize the mechanism of how PREPL modulates Tau phosphorylation.

In recent years, multiomic approaches have been useful in prioritizing and guiding targeted studies. We used a combination of RNA-seq and proteomics profile of PREPL KD cells and identified genes and proteins related to AD that are differentially expressed in PREPL KD cells. Genes and proteins related to synaptic signaling exhibited differential expressions in PREPL KD cells (Fig. 2; Supplemental Tables 2 and 5). For example, annexin A6 (AnxA6), associated with membrane-related events such as vesicle fusion during exocytosis (Croissant et al., 2020), was found to be decreased in PREPL KD cells. The RNA-seq data pointed to downregulation of genes related to cholesterol biosynthesis, and the proteomics data indicated the upregulation of proteins involved in fatty acid degradation (Fig. 2; Supplemental Tables 1 and 2). At the biochemical level, these hydrophobic molecules are backbones of an important posttranslational modification, protein lipidation. Among the protein lipidation processes, palmitoylation is characterized by sorting signal for intracellular protein trafficking (Morello and Bouvier, 1996).

PREPL is found to interact with small molecules characterized to inhibit depalmitoylases (Martin et al., 2011; Lin and Conibear, 2015; Régal et al., 2018). A recent study demonstrated that PREPL functions as a depalmitoylating enzyme (Rosier et al., 2021). Our findings are consistent with this since we find that decreases in PREPL expression lead to increases in protein palmitoylation and that inhibition of PREPL's activity with palmostatin M impairs protein trafficking. This supports a function for PREPL in regulating

protein palmitoylation, consistent with the pleotropic phenotypes in protein trafficking seen with PREPL KD cells.

It is important to highlight that the palmitoylation of proteins studied in this manuscript has been associated with AD pathogenesis. For instance, levels of APP palmitoylation showed an age-dependent increase in mouse brains, which might account for the AD progression during aging (Gelman et al., 2018). In addition, the palmitoylation of SNARE proteins such as SNAP25 and VAMP2 is responsible for their subcellular distribution (Huang et al., 2009), and dysfunction of the SNARE complex is associated with several neurophysiological disorders. Therefore, the molecular changes noticed in PREPL KD cells might be connected to the alteration of total protein palmitoylation levels. Thus, PREPL deficiency in AD may subsequently lead to the deregulation of protein lipidation and ultimately facilitate AD progression. Further studies are needed to 1) identify proteins whose palmitoylation pattern is modulated by PREPL and characterize their involvement in vesicle trafficking and protein processing; 2) examine how changes in protein palmitoylation affect Tau phosphorylation at specific residues to better understand the mechanisms involved in AD pathogenesis; and 3) characterize the impact of PREPL modulation in classic animal models of AD, examining levels of protein palmitoylation in the hippocampus and other brain regions and how this affects learning and memory deficits associated with AD pathogenesis.

Taken together, our results suggest that PREPL might have a pleiotropic function during AD development. Modulation of PREPL expression can affect cell proliferation and the distribution of dense-core vesicles, decrease expression of proteins related to protein processing and secretory pathways, alter synaptic long-term potentiation, increase extracellular Aβ42, and modulate Tau phosphorylation at specific residues. The potential role of PREPL in protein palmitoylation might be the connection for the pleiotropic effects of PREPL knockdown in pathways related to protein processing, trafficking, and synaptic plasticity.

Acknowledgments

The authors thank Mustafa Siddiq in the Department of Pharmacological Sciences for help with confocal microscopy.

Data Availability

The authors declare that all of the data supporting the findings of this study are available within the paper and its Supplemental Material.

Authorship Contributions

Participated in research design: Duarte, Wang, Gomes, Liu, Sharma, Zhang, Devi.

Conducted experiments: Duarte, Wang, Gomes, Liu, Sharma, Fakira, Gupta, Mack.

Performed data analysis: Duarte, Wang, Gomes, Liu, Sharma, Fakira, Gupta, Mack.

Wrote or contributed to the writing of the manuscript: Duarte, Wang, Gomes, Liu, Fakira, Zhang, Devi.

References

Alonso ADC, Mederlyova A, Novak M, Grundke-Iqbal I, and Iqbal K (2004) Promotion of hyperphosphorylation by frontotemporal dementia tau mutations. *J Biol Chem* **279**:34873–34881.

Augustinack JC, Schneider A, Mandelkow EM, and Hyman BT (2002) Specific tau phosphorylation sites correlate with severity of neuronal cytopathology in Alzheimer's disease. *Acta Neuropathol* **103**:26–35.

Beckmann ND, Lin WJ, Wang M, Cohain AT, Charney AW, Wang P, Ma W, Wang YC, Jiang C, Audrain M, et al. (2020) Multiscale causal networks identify VGF as a key regulator of Alzheimer's disease. *Nat Commun* **11**:3942.

Bettens K, Sleegers K, and Van Broeckhoven C (2013) Genetic insights in Alzheimer's disease. *Lancet Neurol* **12**:92–104.

Biernat J, Gustke N, Drewes G, Mandelkow EM, and Mandelkow E (1993) Phosphorylation of Ser262 strongly reduces binding of tau to microtubules: distinction between PHF-like immunoreactivity and microtubule binding. *Neuron* **11**:153–163.

Blitzer RD, Connor JH, Brown GP, Wong T, Shenolikar S, Iyengar R, and Landau EM (1998) Gating of CaMKII by cAMP-regulated protein phosphatase activity during LTP. *Science* **280**:1940–1942.

Brigidi GS and Bamji SX (2013) Detection of protein palmitoylation in cultured hippocampal neurons by immunoprecipitation and acyl-biotin exchange (ABE). *J Vis Exp* **72**:50031.

Bushlin I, Gupta A, Stockton Jr SD, Miller LK, and Devi LA (2012) Dimerization with cannabinoid receptors allosterically modulates delta opioid receptor activity during neuropathic pain. *PLoS One* **7**:e49789.

Cabrales Fontela Y, Kadavath H, Biernat J, Riedel D, Mandelkow E, and Zweckstetter M (2017) Multivalent cross-linking of actin filaments and microtubules through the microtubule-associated protein tau. *Nat Commun* **8**:1981.

Chakraborty TR, Tkalych O, Nanno D, Garcia AL, Devi LA, and Salton SR (2006) Quantification of VGF- and pro-SAAS-derived peptides in endocrine tissues and the brain, and their regulation by diet and cold stress. *Brain Res* **1089**:21–32.

Croissant C, Gounou C, Bouvet F, Tan S, and Bouter A (2020) Annexin-A6 in membrane repair of human skeletal muscle cell: a role in the cap subdomain. *Cells* **9**:1742.

D'Agostino G, Kim JD, Liu ZW, Jeong JK, Suyama S, Calignano A, Gao XB, Schwartz M, and Diano S (2013) Prolyl endopeptidase-deficient mice have reduced synaptic spine density in the CA1 region of the hippocampus, impaired LTP, and spatial learning and memory. *Cereb Cortex* **23**:2007–2014.

Darmanis S, Sloan SA, Zhang Y, Enge M, Caneda C, Shuer LM, Hayden Gephart MG, Barres BA, and Quake SR (2015) A survey of human brain transcriptome diversity at the single cell level. *Proc Natl Acad Sci USA* **112**:7285–7290.

Edmonds MJ, Geary B, Doherty MK, and Morgan A (2017) Analysis of the brain palmitoyl-proteome using both acyl-biotin exchange and acyl-resin-assisted capture methods. *Sci Rep* **7**:3299.

Eichel K and von Zastrow M (2018) Subcellular organization of GPCR signaling. *Trends Pharmacol Sci* **39**:200–208.

Foidl BM and Humpel C (2018) Differential hyperphosphorylation of tau-S199, -T231 and -S396 in organotypic brain slices of Alzheimer mice. A model to study early tau hyperphosphorylation using okadaic acid. *Front Aging Neurosci* **10**:113.

Garcia-Osta A, Tsokas P, Pollonini G, Landau EM, Blitzer R, and Alberini CM (2006) MuSK expressed in the brain mediates cholinergic responses, synaptic plasticity, and memory formation. *J Neurosci* **26**:7919–7932.

Gelman S, Palma J, Tombaugh G, and Ghavami A (2018) Differences in synaptic dysfunction between rTg4510 and APP/PS1 mouse models of Alzheimer's disease. *J Alzheimers Dis* **61**:195–208.

Gupta A, Décaillot FM, Gomes I, Tkalych O, Heimann AS, Ferro ES, and Devi LA (2007) Conformation state-sensitive antibodies to G-protein-coupled receptors. *J Biol Chem* **282**:5116–5124.

Hirosawa M, Hoshida M, Ishikawa M, and Toya T (1993) MASCOT: multiple alignment system for protein sequences based on three-way dynamic programming. *Comput Appl Biosci* **9**:161–167.

Hochberg Y and Benjamini Y (1990) More powerful procedures for multiple significance testing. *Stat Med* **9**:811–818.

Huang K, Sanders S, Singaraja R, Orban P, Cijsouw T, Arstikaitis P, Yanai A, Hayden MR, and El-Husseini A (2009) Neuronal palmitoyl acyl transferases exhibit distinct substrate specificity. *FASEB J* **23**:2605–2615.

Hurd MD, Martorell P, Delavande A, Mullen KJ, and Langa KM (2013) Monetary costs of dementia in the United States. *N Engl J Med* **368**:1326–1334.

Jaeken J, Martens K, Francois I, Eyskens F, Lecointre C, Derua R, Meulemans S, Slootstra JW, Waelkens E, de Zegher F, et al. (2006) Deletion of PREPL, a gene encoding a putative serine oligopeptidase, in patients with hypotonia-cystinuria syndrome. *Am J Hum Genet* **78**:38–51.

Law CW, Chen Y, Shi W, and Smyth GK (2014) Voom: precision weights unlock linear model analysis tools for RNA-seq read counts. *Genome Biol* **15**:R29.

Lechner T, Adlassnig C, Humpel C, Kaufmann WA, Maier H, Reinstadler-Kramer K, Hinterhölzl J, Mahata SK, Jellinger KA, and Marksteiner J (2004) Chromogranin peptides in Alzheimer's disease. *Exp Gerontol* **39**:101–113.

Lemos Duarte M, Trimbake NA, Gupta A, Tumanut C, Fan X, Woods C, Ram A, Gomes I, Bobeck EN, Schechtman D, et al. (2021) High-throughput screening and validation of antibodies against synaptic proteins to explore opioid signaling dynamics. *Commun Biol* **4**:238.

Lin DT and Conibear E (2015) ABHD17 proteins are novel protein depalmitoylases that regulate N-Ras palmitate turnover and subcellular localization. *eLife* **4**:e11306.

Linder ME and Deschenes RJ (2007) Palmitoylation: policing protein stability and traffic. *Nat Rev Mol Cell Biol* **8**:74–84.

Mack SM, Gomes I, Fakira AK, Duarte ML, Gupta A, Fricker L, and Devi LA (2022) GPR83 engages endogenous peptides from two distinct precursors to elicit differential signaling. *Mol Pharmacol* **102**:29–38.

Mansuri MS, Peng G, Wilson RS, Lam TT, Zhao H, Williams KR, and Nairn AC (2020) Differential protein expression in striatal D1- and D2-dopamine receptor-expressing medium spiny neurons. *Proteomes* **8**:27.

Martin BR, Wang C, Adibekian A, Tully SE, and Cravatt BF (2011) Global profiling of dynamic protein palmitoylation. *Nat Methods* **9**:84–89.

Mathys H, Davila-Velderrain J, Peng Z, Gao F, Mohammadi S, Young JZ, Menon M, He L, Abdurrob F, Jiang X, et al. (2019) Single-cell transcriptomic analysis of Alzheimer's disease. *Nature* **570**:332–337.

Matthews KA, Xu W, Gaglioti AH, Holt JB, Croft JB, Mack D, and McGuire LC (2019) Racial and ethnic estimates of Alzheimer's disease and related dementias in the United States (2015-2060) in adults aged ≥65 years. *Alzheimers Dement* **15**:17–24.

Mattsson N, Johansson P, Hansson O, Wallin A, Johansson JO, Andreasson U, Andersen O, Haghighi S, Olsson M, Stridsberg M, et al. (2010) Converging pathways of chromogranin and amyloid metabolism in the brain. *J Alzheimers Dis* **20**:1039–1049.

Millstein J, Zhang B, Zhu J, and Schadt EE (2009) Disentangling molecular relationships with a causal inference test. *BMC Genet* **10**:23.

Morawski M, Nuytens K, Juhasz T, Zeitschel U, Seeger G, Waelkens E, Regal L, Schulz I, Arendt T, Szeltner Z, et al. (2013) Cellular and ultra structural evidence for cytoskeletal localization of prolyl endopeptidase-like protein in neurons. *Neuroscience* **242**:128–139.

Morello JP and Bouvier M (1996) Palmitoylation: a post-translational modification that regulates signalling from G-protein coupled receptors. *Biochem Cell Biol* **74**:449–457.

Nalbantoglu J, Tirado-Santiago G, Lahsaïni A, Poirier J, Goncalves O, Verge G, Momoli F, Welner SA, Massicotte G, Julien JP, et al. (1997) Impaired learning and LTP in mice expressing the carboxy terminus of the Alzheimer amyloid precursor protein. *Nature* **387**:500–505.

Oboudiyat C, Glazer H, Seifan A, Greer C, and Isaacson RS (2013) Alzheimer's disease. *Semin Neurol* **33**:313–329.

Park SA, Han SM, and Kim CE (2020) New fluid biomarkers tracking non-amyloid-β and non-tau pathology in Alzheimer's disease. *Exp Mol Med* **52**:556–568.

Park Y and Kim KT (2009) Short-term plasticity of small synaptic vesicle (SSV) and large dense-core vesicle (LDCV) exocytosis. *Cell Signal* **21**:1465–1470.

Perkins DN, Pappin DJ, Creasy DM, and Cottrell JS (1999) Probability-based protein identification by searching sequence databases using mass spectrometry data. *Electrophoresis* **20**:3551–3567.

Quinn JP, Kandigian SE, Trombetta BA, Arnold SE and Carlyle BC (2021) VGF as a biomarker and therapeutic target in neurodegenerative and psychiatric diseases. *Brain Commun* **3**:fcab261.

Radhakrishnan K, Baltes J, Creemers JW, and Schu P (2013) Trans-Golgi network morphology and sorting is regulated by prolyl-oligopeptidase-like protein PREPL and the AP-1 complex subunit μ1A. *J Cell Sci* **126**:1155–1163.

Régal L, Mårtensson E, Maystadt I, Voermans N, Lederer D, Burlina A, Juan Fita MJ, Hoogeboom AJM, Olsson Engman M, Hollemans T, et al. (2018) PREPL deficiency: delineation of the phenotype and development of a functional blood assay. *Genet Med* **20**:109–118.

Régal L, Shen XM, Selcen D, Verhille C, Meulemans S, Creemers JW, and Engel AG (2014) PREPL deficiency with or without cystinuria causes a novel myasthenic syndrome. *Neurology* **82**:1254–1260.

Ritchie ME, Phipson B, Wu D, Hu Y, Law CW, Shi W, and Smyth GK (2015) Limma powers differential expression analyses for RNA-sequencing and microarray studies. *Nucleic Acids Res* **43**:e47.

Robinson MD and Oshlack A (2010) A scaling normalization method for differential expression analysis of RNA-seq data. *Genome Biol* **11**:R25.

Rosier K, McDevitt MT, Smet J, Floyd BJ, Verschoore M, Marcaida MJ, Bingman CA, Lemmens I, Dal Peraro M, Tavernier J, et al. (2021) Prolyl endopeptidase-like is a (thio)-esterase involved in mitochondrial respiratory chain function. *iScience* **24**:103460.

Sayol-Torres L, Valenzuela MI, Tomasini R, Fernández-Alvarez P, Clemente M, and Yeste D (2021) Prolyl endopeptidase-like (PREPL) deficiency associated with growth hormone deficiency: case report. *J Clin Res Pediatr Endocrinol* DOI: 10.4274/jcrpe.galenos.2021.2021.0128 [published ahead of print].

Selkoe DJ and Hardy J (2016) The amyloid hypothesis of Alzheimer's disease at 25 years. *EMBO Mol Med* **8**:595–608.

Silva S, Miyake N, Tapia C, and Matsumoto N (2018) The second point mutation in PREPL: a case report and literature review. *J Hum Genet* **63**:677–681.

Spires-Jones TL and Hyman BT (2014) The intersection of amyloid beta and tau at synapses in Alzheimer's disease. *Neuron* **82**:756–771.

Subramanian A, Tamayo P, Mootha VK, Mukherjee S, Ebert BL, Gillette MA, Paulovich A, Pomeroy SL, Golub TR, Lander ES, et al. (2005) Gene set enrichment analysis: a knowledge-based approach for interpreting genome-wide expression profiles. *Proc Natl Acad Sci USA* **102**:15545–15550.

Tsokas P, Grace EA, Chan P, Ma T, Sealfon SC, Iyengar R, Landau EM, and Blitzer RD (2005) Local protein synthesis mediates a rapid increase in dendritic elongation factor 1A after induction of late long-term potentiation. *J Neurosci* **25**:5833–5843.

von Zastrow M and Sorkin A (2021) Mechanisms for regulating and organizing receptor signaling by endocytosis. *Annu Rev Biochem* **90**:709–737.

Wang M, Beckmann ND, Roussos P, Wang E, Zhou X, Wang Q, Ming C, Neff R, Ma W, Fullard JF, et al. (2018) The Mount Sinai cohort of large-scale genomic, transcriptomic and proteomic data in Alzheimer's disease. *Sci Data* **5**:180185.

Wang M, Li A, Sekiya M, Beckmann ND, Quan X, Schrode N, Fernando MB, Yu A, Zhu L, Cao J, et al. (2021) Transformative network modeling of multi-omics data reveals detailed circuits, key regulators, and potential therapeutics for Alzheimer's disease. *Neuron* **109**:257–272.e14.

Wang M, Roussos P, McKenzie A, Zhou X, Kajiwara Y, Brennand KJ, De Luca GC, Crary JF, Casaccia P, Buxbaum JD, et al. (2016) Integrative network analysis of nineteen brain regions identifies molecular signatures and networks underlying selective regional vulnerability to Alzheimer's disease. *Genome Med* **8**:104.

Wu X, Zhao X, Puertollano R, Bonifacino JS, Eisenberg E, and Greene LE (2003) Adaptor and clathrin exchange at the plasma membrane and trans-Golgi network. *Mol Biol Cell* **14**:516–528.

Yang Q, Hua R, Qian J, Yi S, Shen F, Zhang Q, Li M, Yi S, Luo J, and Fan X (2020) PREPL deficiency: a homozygous splice site PREPL mutation in a patient with congenital myasthenic syndrome and absence of ovaries and hypoplasia of uterus. *Front Genet* **11**:198.

Zhang B, Gaiteri C, Bodea LG, Wang Z, McElwee J, Podtelezhnikov AA, Zhang C, Xie T, Tran L, Dobrin R, et al. (2013) Integrated systems approach identifies genetic nodes and networks in late-onset Alzheimer's disease. *Cell* **153**:707–720.

Zhang B and Zhu J (2013) Identification of key causal regulators in gene networks, in *Proceedings of the World Congress on Engineering 2013*; 2013 July 3–5; London, UK. **Vol 2**, pp 1309–1312, International Association of Engineers, Hong Kong.

Zhu J, Wiener MC, Zhang C, Fridman A, Minch E, Lum PY, Sachs JR, and Schadt EE (2007) Increasing the power to detect causal associations by combining genotypic and expression data in segregating populations. *PLOS Comput Biol* **3**:e69.

Zucker RS and Regehr WG (2002) Short-term synaptic plasticity. *Annu Rev Physiol* **64**:355–405.

Address correspondence to: Bin Zhang, Icahn School of Medicine at Mount Sinai, 1984 Annenberg Building, Box 1603, New York, NY 10029. E-mail: Bin.Zhang@mssm.edu; or Dr. Lakshmi A. Devi, Icahn School of Medicine at Mount Sinai, 1984 Annenberg Building, Box 1603, New York, NY 10029. E-mail: Lakshmi.devi@mssm.edu